



저작자표시-비영리-변경금지 2.0 대한민국

이용자는 아래의 조건을 따르는 경우에 한하여 자유롭게

- 이 저작물을 복제, 배포, 전송, 전시, 공연 및 방송할 수 있습니다.

다음과 같은 조건을 따라야 합니다:



저작자표시. 귀하는 원저작자를 표시하여야 합니다.



비영리. 귀하는 이 저작물을 영리 목적으로 이용할 수 없습니다.



변경금지. 귀하는 이 저작물을 개작, 변형 또는 가공할 수 없습니다.

- 귀하는, 이 저작물의 재이용이나 배포의 경우, 이 저작물에 적용된 이용허락조건을 명확하게 나타내어야 합니다.
- 저작권자로부터 별도의 허가를 받으면 이러한 조건들은 적용되지 않습니다.

저작권법에 따른 이용자의 권리는 위의 내용에 의하여 영향을 받지 않습니다.

이것은 [이용허락규약\(Legal Code\)](#)을 이해하기 쉽게 요약한 것입니다.

[Disclaimer](#)

이학박사 학위논문

Analytical and Electroanalytical Applications of  
Filamentous Bacteriophages and  
Development of Sensitivity-Tunable Ion Sensing  
Platform based on Reverse Electrodialysis

섬사상 박테리오파지의 분석·전기분석적 응용 및  
역전기투석을 이용한 민감도 조절 가능 이온 측정  
플랫폼의 개발

2019 년 8 월

서울대학교 대학원

화학부 전기분석화학전공

노 지 현



# Abstract

## Chapter 1: Analytical and Electroanalytical Applications of Filamentous Bacteriophages

Filamentous bacteriophage is one of the most highlighted biomaterial, thanks to its unique properties: 1) Easy modification of its major coat protein with genetic engineering and bioconjugation, 2) The regularity of the virions along with large population and fast generation time, and 3) The high aspect ratio, 7 nm in width and 880 nm in length, which make it an excellent biomaterial for nanomaterial applications.

First, filamentous bacteriophages are applied as a scaffold of antibody immobilization for bead-based 3D suspension multiplex immunoassay. The size and the fluorescence signal of virus-tethered gold microbead is measured at a DC impedance-based flow cytometer. The large quantity of antibody loading and flexible movement of filamentous virus enabled signal enhancement, elevating sensitivity by up to 5.7-fold compared to the beads without virus. This system successfully accomplished multiplex immunoassay involving four biomarkers: prostate specific antigen, cardiac troponin I, myoglobin, and creatine kinase MB in undiluted human serum.

Second, filamentous bacteriophages are genetically engineered to display 3,4-dihydroxyl-L-phenylalanine (DOPA) onto the major coat protein, where cobalt oxide-based oxygen evolution catalyst (Co-OEC) are deposited spontaneously. It was demonstrated that the catalyst formed on the virus shows improved durability and decrease oxidation state compared with electrodeposited Co-OEC. The DOPA-displaying virus proposes unconventional way of generating electrocatalysts by introducing DOPA as a nucleation site as well as a dopant for Co-OEC.

## Chapter 2: Development of Sensitivity-Tunable Ion Sensing Platform based on Reverse Electrodialysis

Reverse electrodialysis (RED) is a salinity gradient-based power generation system, of which the output voltage is proportional to the 1) concentration difference between river water and seawater, and 2) the number of stacks comprising RED. Inspired by those features mentioned above, RED-based ion sensing platform is proposed. The cation exchange membranes and anion exchange membranes constituting traditional RED are substituted to home-made ion-selective membranes and reference membranes, which generate sample dependent and independent potential, respectively, and the sensitivity is freely modulated by changing the number of stacks. This sensing platform is integrated with a colorimetric detection system based on polyaniline, which is a well-known electrochromic dye, electrodeposited on one bipolar electrode to display sample concentration-dependent colors. Combined with the colorimetric detection system, the RED-based ion sensing platform serves as a power generator as well as an ion concentration selective signal producer, which realize self-powered and disposable ion sensor with tunable sensitivity.

Keywords: Filamentous Bacteriophage, Bead-based immunoassay, Multiplex analysis, Oxygen evolution reaction catalyst, Reverse electrodialysis, bipolar electrode, ion sensor, sensitivity

Student number: 2014-21240

# Table of contents

Abstract .....	i
Table of contents .....	iii
List of Tables .....	v
List of Figures .....	v
Chapter 1. Analytical and Electroanalytical Applications of Filamentous Bacteriophages .....	1
1.1 Introduction .....	1
1.2. Multiplex immunoassay using virus-tethered gold micro-bead by DC impedance-based cytometry .....	2
1.2.1. Introduction .....	2
1.2.2. Experimental .....	5
1.2.3. Result and Discussion .....	11
1.2.4. Conclusion.....	23
1.3. Chemically Deposited Cobalt-Based Oxygen-Evolution Electrocatalysts on DOPA-Displaying Filamentous Bacteriophages .....	25
1.3.1. Introduction .....	25
1.3.2. Experimental .....	26
1.3.3. Result and Discussion .....	32

1.3.4. Conclusion.....	46
1.4. Genetic engineering of filamentous bacteriophage (fd) for the application in SERS active probe.....	47
1.4.1. Introduction .....	47
1.4.2. Experimental .....	48
1.4.3. Result and Discussion .....	51
1.4.4. Conclusion.....	59
1.5. References .....	60
Chapter 2. Development of Sensitivity-Tunable Ion Sensing Platform based on Reverse Electrodialysis .....	65
2.1. Introduction .....	65
2.2. Experimental .....	66
2.3. Result and Discussion .....	71
2.4. Conclusion.....	95
2.5. References .....	96

## List of Tables

Table 1. The concentration of four antigens that tested for multiplex immunoassay with virus-bead in human serum .....	22
Table 2. Primers 1-4 used to create inserts.....	29
Table 3. Primer 1-4 for the genetic engineering of filamentous bacteriophage .....	48
Table 4. The result of sequencing of 10 randomly picked colonies of filamentous bacteriophage.....	57
Table 5. Sensitivity of MISM as a function of the number of stacks. Nitrate concentrations from 0.02 mM to 5 mM were used to plot the trend line for sensitivity of each stack.....	81
Table 6. Results of river water analysis.....	94

## List of Figures

Fig. 1-1. Schematic process of multiplex immunoassay targeting four antigens.....	4
Fig. 1-2. Surface modification process of virus-tethered gold bead.....	12
Fig. 1-3. Optimization of the concentration of DBCO-sulfo-NHS. ....	12
Fig. 1-4. Comparison of SAV-bead with Virus-bead, when antibodies are conjugated maximally.....	14



Fig. 1-5. Histogram of the impedance obtained from two different diameters of Au-micro-beads. ....	16
Fig. 1-6. Representative DC impedance change and fluorescence signals from multiplex immunoassay of four different antigens in human serum. ....	17
Fig. 1-7. Sandwich-immunoassay profiles are presented for four different antigens.....	20
Fig. 1-8. Multiplex immunoassay profile in human serum .....	22
Fig. 1-9. Optimization of Co/DOPA-phages. ....	30
Fig. 1-10. TEM and SEM images and XP spectra of Co/DOPA-phages.	33
Fig. 1-11. The 10-cycles of Cyclic voltammograms on GC RDE to stabilize Co/DOPA-phages. ....	35
Fig. 1-12. Consecutive cyclic voltammograms of Co/DOPA-phages and he Raman spectra of Ed-Co and Co/DOPA-phages. ....	36
Fig. 1-13. Consecutive cyclic voltammograms for OER using Ed-Co. ...	37
Fig. 1-14. Electrochemical activity of Co/DOPA-phages. ....	40
Fig. 1-15. Electrocatalytic oxidation of $\text{Co}^{2+}$ ions dissolved in electrolyte on phages-modified and bare GC electrodes.....	41
Fig. 1-16. The binding energies between 50~58 eV in Co/DOPA-phages and Ed-Co.....	41
Fig. 1-17. Durability test of Ed-Co and Co/DOPA-phages. ....	44
Fig. 1-18. Stability of Co/DOPA-phages modified RDE. ....	44

Fig. 1-19. Stability of phage under OER condition.....	45
Fig. 1-20. The PCR products and DNA cuts are analyzed with EtBr gel-electrophoresis.....	52
Fig. 1-21. The PCR products and DNA cuts are analyzed with EtBr gel-electrophoresis. The higher concentration of template DNA result in brighter bands.....	52
Fig. 1-22. The result of sequencing of DNA with random sequences.....	53
Fig. 1-23. The absorption spectrum of filamentous bacteriophage (a) before and (b) after centrifugation.....	56
Fig. 1-24. Acceptor peptide expressed at p3 is verified with western blot. ....	58
Fig. 1-25. The Raman shift from (a) genetically engineered phage and (b) wild type phage. ....	58
Fig. 2-1. Schematic illustration of MISM and its electrical profile.....	73
Fig. 2-2. FESEM images of Membranes.....	73
Fig. 2-3. Measurement of membrane charge density of DM.....	74
Fig. 2-4 . Characteristics of DM with different MWCO. ....	75
Fig. 2-5. Membrane potential of DMs with different MWCO.....	77
Fig. 2-6. Characteristics and emf enhancement of MISM.....	78
Fig. 2-7. Voltage distribution of 1 stack (top) and 2 stack MISM (bottom) for nitrate concentration of 0.1 mM (red) and 0.12 mM (black). ....	79

Fig. 2-8. emf enhancement of MISM with NSM and CSM .....	82
Fig. 2-9. The potential of a 6 stack MISM reaches $\pm 1$ mV of the stabilized value within 5 s after the injection of the electrolyte, and the potential decreases 1.3% in 30 s on average. ....	83
Fig. 2-10. Stability of single stack MISM. ....	83
Fig. 2-11. Structure and the color of BPE-based colorimetric detection system.....	85
Fig. 2-12. Cyclic voltammogram of polyaniline that has four oxidation states and respective colors. ....	86
Fig. 2-13. Hue value, Pixel intensity, and color chart according to applied potential.....	88
Fig. 2-14. Combined structure and Hue value of MISM and BPE-based sensor.....	89
Fig. 2-15. Resistance of MISM .....	92
Fig. 2-16. Hue value and colors of PANi corresponding to the nitrate concentration. ....	93
Fig. 2-17. Photographs of a single stack MISM and BPE microchip.....	94

# Chapter 1. Analytical and Electroanalytical Applications of Filamentous Bacteriophages

## 1.1 Introduction

Since phage display technology was first reported by George P. Smith in 1985, it has played an important role in antibody development. Filamentous bacteriophages are virus of bacteria, and its well-known strains (M13, f1, fd) has almost identical biological and structural characteristics. [1] Filamentous bacteriophage are defined by its long and rod-like shape (~6 nm in width, 880 nm in length), where single-stranded DNA is enclosed by capsid, which is composed of the ~2700 copies of major coat protein (p8), along with few copies of minor coat protein. [2] Filamentous bacteriophage received great attention as a new nanomaterial due to its characteristics: 1) Capsid is easily modified by genetic engineering, exposing high copies of functional groups by p8-targeted engineering, or site-specific exposure by minor coat protein engineering. 2) The regular, controllable length and width of filamentous bacteriophage with high aspect ratio, along with easy amplification and purification of the virion copies. 3) Biocompatible, highly stable and robust nature of filamentous bacteriophage. Many applications with filamentous bacteriophage are reported, taking advantages of those features mentioned above. The large surface area of filamentous bacteriophage is actively exploited at the early stage of material application, for example, as anodic material for lithium ion battery, [3] enhanced electrocatalyst for water reduction, [4] flexible nanogenerator, [5] and so on. As a biocompatible material with easy incorporation of various functional group, bacteriophage was used as a cell guidance, [6] scaffold for bone regeneration, [7]

and so on. Chemical functionalization of virus requires mild and facile chemoselective reaction. [8] Chemical functionalization on filamentous bacteriophage frequently utilize amino group (N-terminal and lysine), and carboxyl group (glutamic acid and aspartic acid) of major coat protein. For more selective and specific reaction, tyrosine, and serine or threonine is involved in chemical reactions.

Filamentous bacteriophage is used in analytical and electroanalytical applications as a vaccine carrier, recognition molecule, and cancer cell imaging. M13 is coated with metal precursors and used as a template for enzymatic glucose biosensing, [9], [10] and engineered to expose specific peptides to recognize various bacteria including salmonella, and human serum albumin. [11]–[13] The combination of simple, cheap electrochemical method and high specific and easy mass production of filamentous bacteriophage is considered as a good approach. [14] Although application of filamentous bacteriophages over last decades have been splendid, it needs collaborative approach for the future of the filamentous bacteriophage-based system.

## 1.2. Multiplex immunoassay using virus-tethered gold micro-bead by DC impedance-based cytometry

### 1.2.1. Introduction

The importance of on-field analysis is growing, and high-throughput and portable bioanalytical system is on demand. [15], [16] Multiplex and bead-based suspension array can effectively realize the merits of intrinsic testing. There are several challenges remaining, for competitive multiplex immunoassay methodology, including effective prevention of nonspecific adsorption, enhanced sensitivity, and

smaller instrument for point-of-care use. It is known that self-assembled monolayer (SAM) can prevent non-specific binding, when it is combined with hydrophilic functional groups such as polyethylene glycol (PEG). [17]–[19] The PEG-SAM on gold microbead is shown to prevent non-specific binding compared to commercial polymer beads in human serum.

The microfluidic chip-based readout device is widely used as bead-based suspension immunoassay, instead of traditional fluorescence-activated cell sorting (FACS), especially for point-of-care application [20]–[22]. Although the chip itself is favorable for miniaturization, the light scattering compartment requires sizable space and sophisticated alignment. It was previously reported that the size of the bead could be measured with DC impedance instead of scattered light, and showed fully integrated chip-based instrument, which showed enhanced portability. [23], [24]

Filamentous bacteriophage is immobilized on the surface of gold micro-bead in orientation-controlled manner, by genetically engineering its viral terminal (p3). Immobilization of filamentous bacteriophage with its viral terminus (p3 or p7 protein) is especially intriguing, in that the free movement of filaments is guaranteed and the side of the filamentous structure, which corresponds to most of the surface area of virus, is maximally available. In this work, filamentous bacteriophage is immobilized on the surface of gold micro-beads in an orientation-controlled manner, and verified its feasibility in a multiplexed immunoassay with a miniaturized DC impedance-based microfluidic flow cytometer as a detection system. The enhanced antibody loading on virus-tethered bead is compared with beads without virus. Four human oriented proteins, *i.e.* cardiac troponin I (cTnI), creatine kinase MB (CK-MB), prostate specific antigen (PSA), and myoglobin is analyzed in undiluted human serum. With the combination of beads with two different size (10 and 15  $\mu\text{m}$ ) and two different fluorophore, four antigens are distinguished simultaneously. (Fig. 1-1)

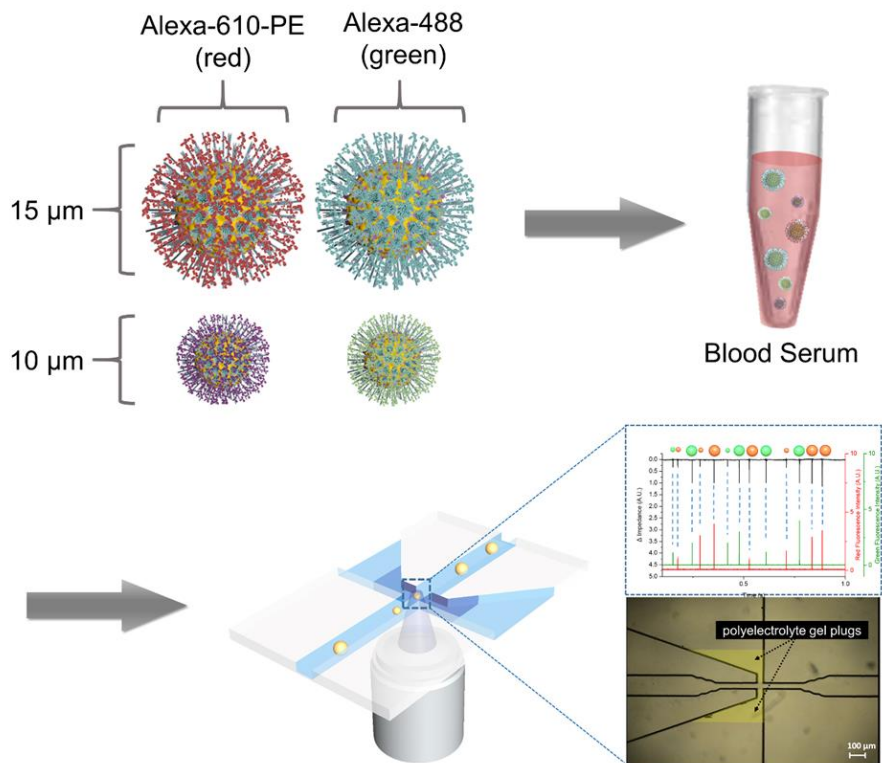


**Fig. 1-1. Schematic process of multiplex immunoassay targeting four antigens.**

## 1.2.2. Experimental

### 1.2.2.1. Materials

SfiI and NotI were purchased from New England Biolab (Ipswich, MA, USA). Biotin PEG thiol was purchased from Polypure AS (Oslo, Norway). Biotin, biocytin Alexa Fluor 488, Alexa Fluor 488-azide, NHS-PEG4-azide, goat anti-rabbit Alexa Fluor 610-PE, chicken anti-rabbit Alexa Fluor 488, streptavidin conjugated with horseradish peroxidase (SAV-HRP), sea block blocking buffer were purchased from ThermoFisher Scientific (Waltham, MA, USA). Mouse IgG, 3,3',5,5'-tetramethylbenzidine (TMB)-liquid substrate system, bovine serum albumin (BSA), PSA from human serum, streptavidin, tetracycline (Tet), Human serum from human male AB plasma, poly(ethylene glycol) with Mn 8000, NaCl >99.5 % were purchased from Sigma-Aldrich (St. Louis, MO, USA). Dibenzocyclooctyne-sulfo-N-hydroxysuccinimidyl ester (DBCO-sulfo-NHS) was purchased from Click Chemistry Tools (Scottsdale, AZ, USA). Creatine kinase (CK)-MB antibodies, cardiac troponin I (cTnI) antibodies, myoglobin antibodies, prostate specific antigen (PSA) antibodies, donkey anti-goat alexa fluor 488, rabbit anti-fd, donkey anti-sheep alexa fluor 488, cardiac troponin I protein, myoglobin protein were purchased from Abcam (Cambridge, England). CK-MB protein was purchased from Fitzgerald (Acton, MA, USA). Electrocompetent TG1 was purchased from Lucigen (Middleton, WI, USA). fd-tet vector was purchased from Invitrogen (Carlsbad, CA, USA). Gold layered on poly(methylmethacrylate) (PMMA) microspheres with two different diameters (10  $\mu\text{m}$  and 15  $\mu\text{m}$ ) were purchased from Nomadien. Dulbecco's phosphate-buffered saline (DPBS) (pH 7.3) was purchased from Welgene (Korea). Amicon ultra centrifugal filter with MWCO 10 kDa was purchased from Millipore (Billerica, MA, USA). Slide glasses were purchased from Marienfeld (Lauda-Königshofen, Germany). Hexamethyldisilazane (HMDS), AZ4620 and AZ400K



were purchased from Merck (Kenilworth, NJ, USA). UV aligner was purchased from Midas System (Daejeon, Korea). Buffered oxide etch (BOE) 6:1 solution was purchased from J. T. Baker (PA, U.S.A.). Furnace (CRF-M15) was purchased from DAIHAN Scientific (Korea). 3-(trimethylsilyl) propyl methacrylate (TMSMA), diallyl dimethylammonium chloride (DADMAC), 2-hydroxy-40-(2-hydroxyethoxy)-2-methylpropiophenone, N,N'-methylene-bisacrylamide, and potassium chloride was purchased from Sigma-Aldrich (St. Louis, MO, USA). Ar laser (150m) was purchased from LASERPHYSICS (UT, U.S.A.). Optical filters were purchased from Thorlabs (Newton, NJ, USA.). Photomultiplier tubes (PMT) were purchased from Hamamatsu (Shizuoka Pref., Japan). Syringe pump (KDS 200) was purchased from KD Scientific (Holliston, MA, USA). 100 µm diameter capillaries (Polymicro Technologies) were purchased from Molex (Lisle, IL, USA). NanoPort Assemblies were purchased from IDEX Health & Science (Oak Harbor, WA, USA)

#### 1.2.2.2. Filamentous bacteriophage with acceptor peptide (AP)

The fd-tet vector was cut by SfiI and NotI and the inserts were created by polymerase chain reaction (PCR) using two primers, AP-F (5' -CGG CCA TGG CAG GTC TGA ACG ACA TCT TCG AGG CTC AGA AAA TCG AAT GGC ACG AAG GCT CCG GTG C-3') and AP-R (5' -GGC CGC ACC GGA GCC TTC GTG CCA TTC GAT TTT CTG AGC CTC GAA GAT GTC GTT CAG ACC TGC CAT GGC CGG CT-3'). After the vector construct was verified by DNA sequencing, it was transformed into electrocompetent TG1 cells and plated on lysogeny broth (LB) containing 20 µg mL<sup>-1</sup> of tetracycline (tet). After 1 day, single colony was selected to be grown in 400 mL of NZY/tet (20 µg mL<sup>-1</sup>) growth media overnight at 37 °C. E. coli were removed from cell culture media by centrifugation at 12,000 g for 10 minutes. The supernatant was thoroughly mixed with 1/5 volume of PEG/NaCl and

incubated at 4 °C to be centrifuged at 16,000 g for 20 minutes the next day. The precipitated phages were resuspended in PBS buffer (pH 7.3) and their concentration verified by spectroscopic method.

#### 1.2.2.3. Optimization of azide conjugation

50 mg of mouse IgGs was incubated with 0.2 mM, 0.5 mM, or 1 mM of NHS-PEG4-azide for 1 hour. The unreacted NHS-PEG4-azide was removed using centrifuge filtration for four times, and 0.5 mg of azide-modified antibody was conjugated to ~1000 DBCO-immobilized SAV beads for 3 hours at RT. The antibody-modified microspheres were incubated with 0.5 mg of anti-mouse from rabbit Alexa 594 for 30 minutes and then washed 3 times with PBS. It was identified that the difference of MFI between 0.2 mM and 0.5 mM was within the detecting instrument's error range, and the MFI of the 1 mM azide sample was 12.4 % lower than the MFI seen for the concentration of 0.2 mM and 0.5 mM.

#### 1.2.2.4. DBCO conjugation on microbead

~35,000 beads were incubated with 0.25 mM (SAV beads) or 2 mM (virus-beads) of DBCO-sulfo-NHS for 30 minutes at RT. The unreacted chemicals were washed away with DPBS, and azide-modified antibodies were conjugated with DBCO-modified beads for 3 hours at RT.

#### 1.2.2.5. Surface modification of gold micro-bead

1 mg of Au-layered microspheres (~500,000 beads) were incubated with 1 mM of biotin-terminated deca(ethylene glycol) thiol SAM in ethanol for 1 hour. The beads were washed with DPBS 3 times and stored at 4 °C. ~35,000 beads were incubated with SAVs (20 mg) for 40 minutes. The unreacted SAVs were washed three times with DPBS. The SAV-beads were either conjugated with various azide-modified

antibodies after reaction with DBCO-sulfo-NHS, or conjugated with virus. For virus conjugation, the SAV-beads were blocked with 1 % BSA for 10 minutes, at RT, and further incubated with  $5.0 \times 10^{12}$  phage virions for 16 hours, at 4 °C.

#### 1.2.2.6. Immunoassay

After antibody modification, SAV-beads or virus-beads were blocked with undiluted sea block blocking buffer for 10 minutes at RT. The blocking buffer was removed by centrifugation, and various concentrations of antigen in undiluted human serum were incubated with the beads for 10 minutes at RT. For multiplex immunoassays, three other antigens at a concentration of 1 mg mL<sup>-1</sup> were co-incubated with the target. The beads were washed with DPBS for 3 times, and 0.5 mg of primary antibodies against the target was incubated with the beads for 5 minutes at RT, followed by washing with DPBS for 3 times. For multiplex immunoassays, 0.5 mg of primary antibodies against the three other antigens was co-incubated. After 0.5 mg of anti-goat 488 and anti-sheep 488 fluorescent antibodies were incubated with the beads for 5 minutes and washed away, 0.5 mg of anti-rabbit 610 PE antibody was incubated with the beads for 5 minutes at RT, and the fluorescence was analyzed with microfluidic chip.

#### 1.2.2.7. Fluorescence microscopy

Fluorescence was monitored using IX71 (Olympus) equipped with DXM-1200C CCD camera (Nikon). Au microspheres in 5 µl of PBS were spotted onto glass microscope slide. At least 20 microspheres were chosen and the mean fluorescence intensity (MFI) was analyzed using NIS-Elements software version 2.30 (Nikon).

#### 1.2.2.8. Fabrication of a microfluidic chip

A microfluidic glass chip was fabricated by similar photolithographic techniques to those described in our previous reports. [23], [25] Briefly, glass slides were immersed in piranha solution ( $\text{H}_2\text{SO}_4:\text{H}_2\text{O} = 3:1$ ) for 30 minutes, then rinsed with deionized (DI) water and dried with an air blow gun. HMDS was spin-coated onto cleaned slides at 7000 rpm for 30 seconds. The HMDS-coated slides were placed on a hot plate at  $120^\circ\text{C}$  for 3 minutes. Afterwards, the photoresist (PR) AZ4620, was spin-coated onto the surface of the slides using a spin coater at 7000 rpm for 30 seconds. The PR-coated slides were placed on a hot plate at  $100^\circ\text{C}$  for 1.5 minutes. The slides were aligned under a film photo mask, and exposed to UV light (365 nm,  $18 \text{ mJ cm}^{-2}$ ) for 22 seconds with a UV aligner. The UV-exposed slides were developed using AZ400K developer. The slides were then cleaned with DI water and dried with an air blow gun. Next, the slides were hard-baked at  $150^\circ\text{C}$  for 15 minutes. After cooling to RT, the slides were etched for 33 minutes using 6:1 buffered oxide etch (BOE) solution. The non-patterned slides were drilled for creating inlet and outlet holes using 1mm drill bit, followed by thermal bonding to the patterned glass in a furnace.

Polyelectrolyte gel plugs were fabricated inside the microfabricated channels for measuring DC impedance changes, as described in our previous reports. [23], [25] Briefly, the surfaces of the microfluidic channels were coated with TMSMA to improve adhesion of the polyelectrolyte gel plugs. Next, the microfluidic channels were filled with a monomer solution that consisted of DADMAC, 2% photoinitiator (2-hydroxy-40-(2-hydroxyethoxy)-2-methylpropiophenone), and 2% cross-linker (N,N'-methylene-bisacrylamide). The desired polyelectrolyte gel plug area was exposed to UV light (365 nm) under the film photo mask. Then, polyelectrolyte gel

plugs were fabricated only in the UV-exposed microfluidic channels, and the remaining monomer solution was removed with 1 M KCl.

#### 1.2.2.9. Chip-based immunoassay

An external custom-made circuit generated a 0.8 V DC bias applied between two Ag/AgCl electrodes and detected the impedance change between the polyelectrolyte gel plugs on the microfluidic chip. The DC impedance-analyzing circuit removed the DC component, and then the impedance signal was amplified by operational amplifier components. For the simultaneous measurement of fluorescence and DC impedance, an Ar laser (488 nm) was focused on the detection region in between the polyelectrolyte gel plugs by an objective lens (40 ×, Nikon). The fluorescence signal was optically filtered by 530/43 and 620/52 nm band-pass filters and detected by PMT. The impedance and fluorescence signals were transmitted through the DAQ card (USB-X-6356, National Instruments) with 10 kHz sampling rates. The signals of beads were saved and matched by using a self-programmed LabVIEW (LabVIEW 2015, National Instrument) program. The averages and standard deviations of each concentration were calculated by triple measurement of the mean fluorescence intensity.

The beads and PBS were withdrawn from the outlet by a syringe pump (KDS 200, KD Scientific Inc.) with a flow rate of 10 mL min<sup>-1</sup>. To generate bottom sheath flow, DPBS solution in a reservoir was located back of the sample inlet. The syringe pump and microfluidic chip were connected by 100 μm diameter capillaries with Nano Port Assemblies (Upchurch).

### 1.2.3. Result and Discussion

#### 1.2.3.1. Characterization of virus-tethered gold micro-bead

Virus-tethered gold micro-beads are prepared similar to the previous report on fabrication of biomimetic architectures on gold micro-beads. (Figure 1-2) [26] In this work, detailed characteristics of virus-beads are identified to figure out the role of virus filaments on the multiplexed immunoassay application. Furthermore, several technical improvement was made including substituting Staudinger ligation to strain-promoted azide-alkyne cyclic addition using dibenzocyclooctyne (DBCO) and azide, which is much faster than Staudinger ligation, for bio-orthogonal chemical ligation between antibodies and phages. In addition, in vivo biotinylation of p3 was further optimized to make in vitro biotinylation obsolete. [27]

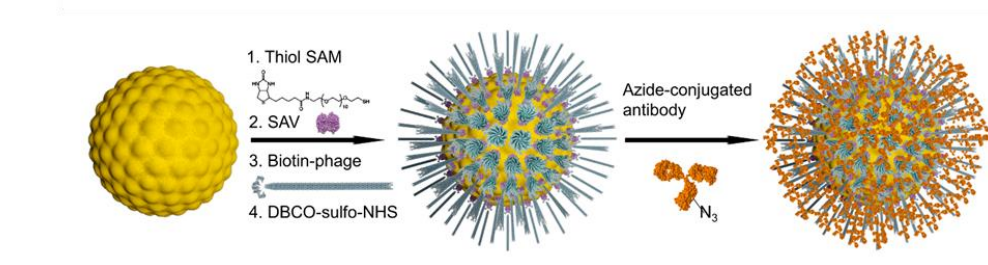


**Fig. 1-2. Surface modification process of virus-tethered gold bead.**

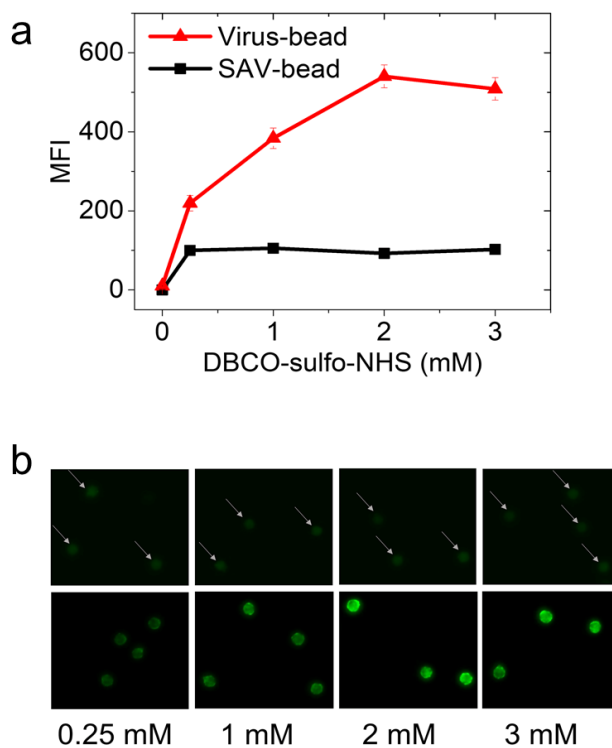


**Fig. 1-3. Optimization of the concentration of DBCO-sulfo-NHS.**

a. optimization between virus-beads and SAV-beads. b. fluorescence of SAV-beads (upper panel) and virus-beads (lower panel)

First of all, I optimized the concentration of DBCO-sulfo-NHS for maximal covalent modification of amine groups on SAV- and virus-loaded microbeads, respectively. As expected, when I measured the degree of chemical modification using Azide-Alexa Fluor 488, the fluorescence plateaued at higher concentration of DBCO-sulfo-NHS in the case of virus-tethered microbeads (2 mM) when compared to SAV-microbeads (0.25 mM), which have less amine groups available for DBCO-sulfo-NHS conjugation (Fig. 1-3 a). Given that the fluorescence intensity increases linearly before saturation, the virus-beads have roughly five-times more DBCO terminals available for azide-fluorophore conjugation compared to SAV-beads. When both beads were maximally treated with azide-conjugated Mouse IgGs, the fluorescence difference between SAV-bead and virus-bead was decreased to 3.3 fold (Fig. 1-4 a).

The amount of antibody loading on SAV-beads and virus-beads was reconfirmed using absorption spectrometry. HRP-conjugated anti-mouse IgGs were captured by mouse IgG-conjugated SAV-beads or virus-beads, followed by incubation with 3,3',5,5'-tetramethylbenzidine (TMB)-hydrogen peroxide solution for the measurement of absorbance at 370 nm. [28] The number of HRP-conjugated antibodies on beads were estimated to be 0.97 pg for SAV-beads and 3.62 pg for virus-beads (3.7 fold difference) by the correlation between the absorption and the concentration of the HRP-antibody. The difference between SAV- and virus-beads is similar to the one obtained using antibody-fluorophore (3.3 fold) and smaller than the one using azide-fluorophore (5 fold), supposedly due to the size difference between azide-fluorophore (~1 kDa) and antibody-fluorophore (~150 kDa).



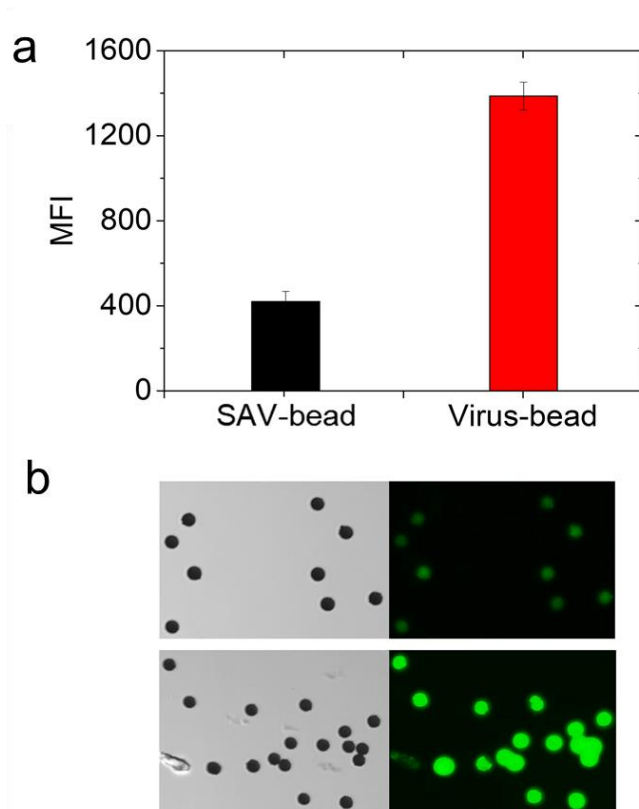


**Fig. 1-4. Comparison of SAV-bead with Virus-bead, when antibodies are conjugated maximally.**

a. The MFI from anti-mouse IgG Alexa fluor 488 of SAV-beads and virus-beads after mouse-IgG was maximally conjugated on each bead. b. The mouse-IgG conjugated SAV-bead (upper panel) and virus-bead (lower panel) were visualized with anti-mouse IgG Alexa Fluor 488.

### 1.2.3.2. Detection of specificity using DC-impedance based chip cytometry

The feasibility of conducting suspension array-based multiplex detection was investigated with four different antigens (cTnI, CK-MB, PSA, and myoglobin) in untreated human serum, and the sensitivity was compared between virus-bead and SAV-bead. Micro-bead in diameter of 15  $\mu\text{m}$  was used for cTnI and CK-MB, and Alexa Fluor 488 and Alexa Fluor 610-R-PE was used to define the concentration of each antigen, respectively. Alexa Fluor 488 and Alexa Fluor 610-R-PE share the excitation wavelengths, which make it easier to simplify the detection part of chip-based flow cytometer with single lightsource. Likewise, for myoglobin and PSA I chose 10  $\mu\text{m}$  beads in common, and Alexa Fluor 488 and Alexa Fluor 610-R-PE, respectively. Thus the combination of the two different fluorescence channels and the two different bead sizes is sufficient for the multiplex detection of four different biomarkers.

For simultaneous measurement of bead size and fluorescence, I monitored DC impedance changes at the spot between two polyelectrolytic gel plugs in the the microfluidic network, where the laser focal plane is also located (See Fig. 1-1). Given the dimension of the microchannel, it is possible for more than one smaller microbeads can pass together to give greater false-positive impedance signals and vice versa. Therefore, I analyzed impedance distribution profiles of the two different types of microbeads and individually gated to rule out size overlaps occurring between 0.3 and 0.5 of apparent impedance (Fig. 1-5). To improve our previous work and others, I implemented an asymmetric inlet to reduce particle clogging and a dual-inlet producing bottom layer flow to minimize beads sedimentation at the sample inlet. [29], [30] With this setup, the efficiency of bead loading could rise, especially for 15  $\mu\text{m}$  beads (data not shown).

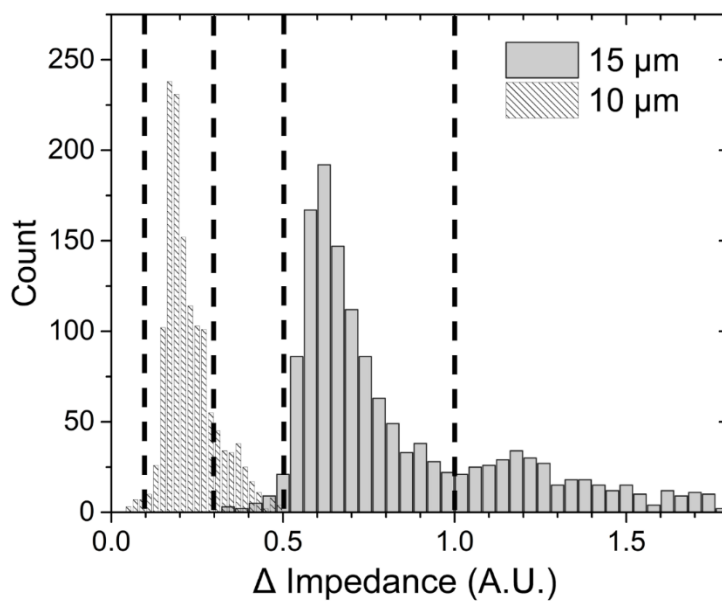


**Fig. 1-5. Histogram of the impedance obtained from two different diameters of Au-micro-beads.**

To discriminate the population of singlet beads for each diameter, the impedance of beads was gated as 0.1~0.3 and 0.5~1.0 for 10  $\mu\text{m}$  and 15  $\mu\text{m}$ , respectively.

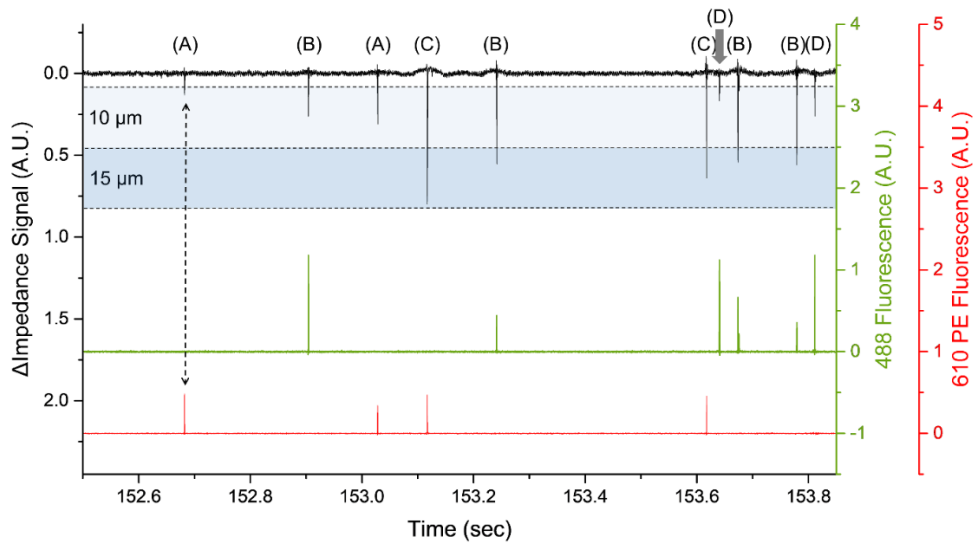


**Fig. 1-6. Representative DC impedance change and fluorescence signals from multiplex immunoassay of four different antigens in human serum.**

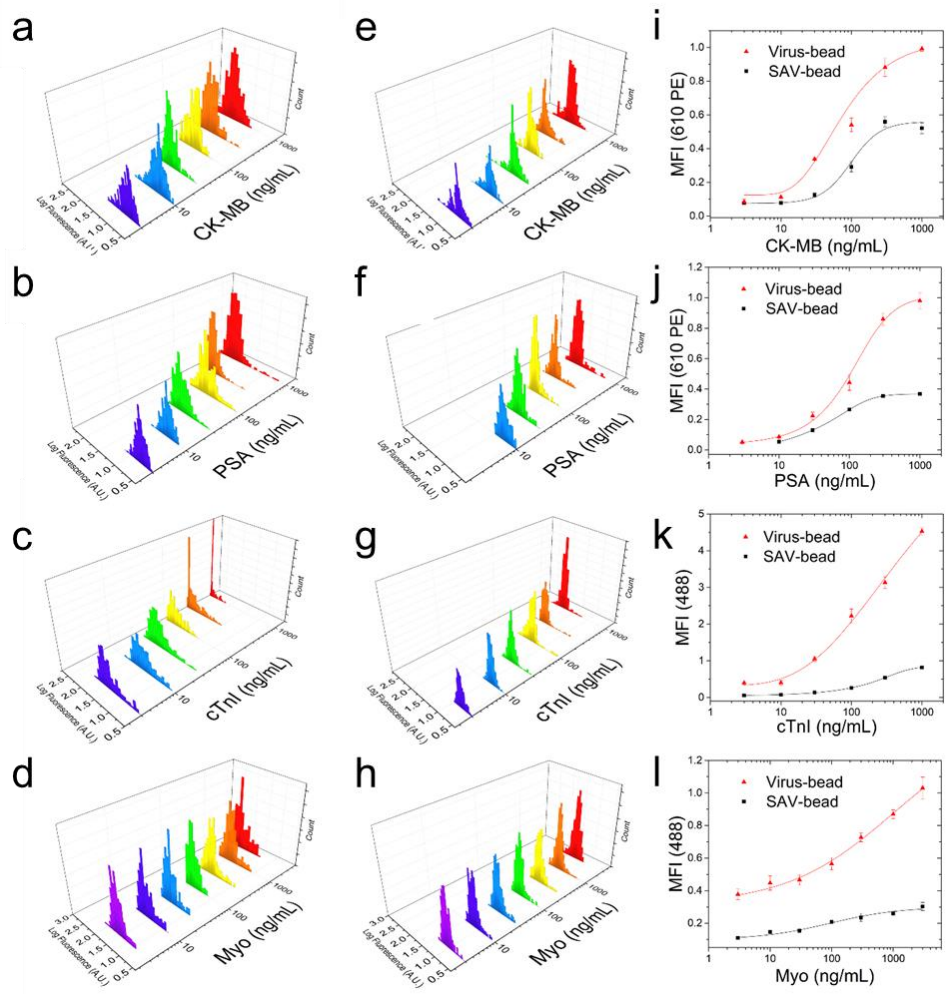
∠ Impedance signals included in blue and darker blue zones correspond to 10 μm and 15 μm beads, respectively. The impedance peaks (black) synchronized with either Alexa Fluor 488 (green) or the Alexa Fluor 610-R-PE (red) fluorescence signals, indicating one of four antigens, i.e. (A) PSA, (B) myoglobin, (C) CK-MB, (D) cTnI. The background signals were trimmed out for simplicity.

Fig. 1-6 shows one of the typically observed data of  $\Delta DC$  impedance and dual fluorescence signals, which is the result of multiplex immunoassay of four different antigens in one pot. The  $\Delta DC$  impedance depends on the size of the bead passing between polyelectrolyte gels, smaller amplitudes for 10  $\mu m$  bead and bigger amplitudes for 15  $\mu m$  bead. Each impedance signal is synchronized with one of fluorescence signal peaks, with either Alexa Fluor 488 or Alexa Fluor 610-R-PE, and the amplitude of the fluorescence signal corresponds to certain concentration of antigen that could be calculated from calibration curve. For example, the first bead from Fig. 1-6 that appears around 152.7 second shows impedance peak of 10  $\mu m$  and fluorescence signal of 610-R-PE, indicating that it's a bead with anti-PSA antibodies conjugated, with the fluorescent intensity matching for certain concentration of PSA in serum. The collective result of multiplexed immunoassay is analyzed in section 1.2.3.4.

#### 1.2.3.3. Signal-enhancement in virus-bead based immunoassay

The calibration curves for four different antigens that were acquired from microfluidic chip is shown in Fig. 1-7. The number of beads collected for each concentration of antigen was fixed to 100 to secure both time and accuracy of immunoassay. The distributions of fluorescence in relation to the concentration of each four antigens of virus-beads are shown in Fig. 1-7 a-d and that of SAV-beads are shown in Fig. 1.7 e-h. The center of the distribution of fluorescence gradually increases within the detection region, and the standard deviation of virus-bead and SAV-bead was 5.72 % and 5.29 % of MFI on average, respectively. In every antigen, the fluorescence signal was notably enhanced in virus-tethered beads compared to SAV-modified beads, and the effect of filamentous virions on beads was most

striking in cTnI with 5.7-fold increase of sensitivity (calculated by slope from the linear range of the calibration curve). Even for other antigens, sensitivities are increased 1.7, 2.6, and 3.8-fold for CK-MB, PSA, and myoglobin, respectively. The differences in enhancement by virus-beads among antigens may originate from the intrinsic properties of protein-protein interactions such as binding constant, size, and structure. [31], [32] SAV-beads with PSA antigen below the concentration of 3 ng mL<sup>-1</sup> was not able to be distinguished from the background. The signal enhancement of virus-bead compared to SAV-bead is especially powerful when the fluorescence intensity is buried by the instrumental background noise in low-concentration range, as it is shown in PSA. It is noteworthy that the enhancement of assay performance by virus-beads is greater than the augmentation in antibody loading on virus-beads (see Fig. 1-4). The non-linear assay enhancement of virus beads could be due to the flexible and free movement of filamentous structures of virus, which mimics the heritage of natural evolution found in a variety of biological systems.



**Fig. 1-7. Sandwich-immunoassay profiles are presented for four different antigens.**

The right-most column (i, j, k, l) shows the calibration curve derived from fluorescence histogram of SAV-bead (black) and Virus-bead (red). The distribution of fluorescence according to the different concentration of antigen in human serum is presented for virus-bead (a, b, c, d) and SAV-bead (e, f, g, h)

#### 1.2.3.4. Feasibility of multiplex immunoassay using Virus-Tethered Gold Microspheres by DC Impedance-based Flow Cytometry

Fig. 1-8 shows the calibration curve for each antigen in the presence of other three antigens in human serum, which evaluates the validity of this system in the situation of multiplex immunoassay. The deviation of MFI between the calibration curves with and without other three antigens is 4.8 % in average. As it was verified that the dense PEG-SAM on gold-layered microspheres could effectively prevent non-specific adsorptions on the beads, the low percentage deviation is likely to result from the protection of the bead with PEG-SAM. [33] For multiplex immunoassay, four different virus-tethered microspheres conjugated with PSA, myoglobin, cTnI, and CK-MB were incubated with randomly chosen concentration of those four antigens in one single pot. The result was analyzed with 3D coordinate system for Alexa Fluor 488, Alexa Fluor 610-R-PE, and impedance (Fig. 1-8 b). It is clear that virus-beads with PSA and myoglobin, which is 10  $\mu\text{m}$  in diameter are well distinguishable from virus-beads with CK-MB and cTnI, which are 15  $\mu\text{m}$  in diameter. Virus-beads capturing myoglobin and cTnI showed no spillover to Alexa Fluor 610-R-PE emission region, and virus-beads for CK-MB and PSA shows little signals in Alexa Fluor 488 emission wavelength. The concentration of each antigen and the percentage error are presented in Table 1-1.



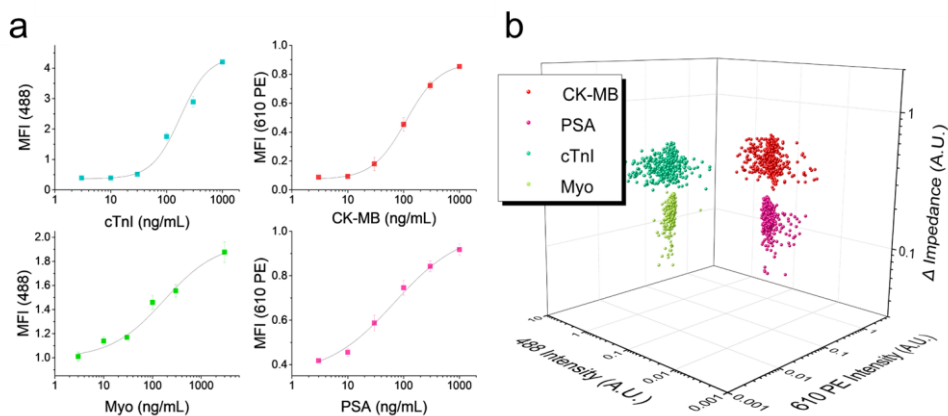


**Fig. 1-8. Multiplex immunoassay profile in human serum**

a. Sandwich immunoassay profiles with virus-beads from multiplex detection environment in human serum for each antigen. b. The result of multiplex immunoassay with virus-beads in human serum with the combination of four different concentration of antigens are presented in 3D-scatter plot.

**Table 1. The concentration of four antigens that tested for multiplex immunoassay with virus-bead in human serum**

Antigen	CK-MB	cTnI	PSA	myoglobin
Concentration [ $\text{ng mL}^{-1}$ ]	100	3	10	300
MFI from calibration curve [A.U.]	0.4534	0.3922	0.4557	1.555
MFI measured [A.U.]	0.4327	0.3875	0.4849	1.493
Percentage error [%]	4.565	1.198	6.407	3.987

#### 1.2.4. Conclusion

Multiplexed and miniaturized immunoassay system is essential for futuristic point-of-care diagnostics. Bead-based immunoassay system is a promising candidate because of its requirement of small sample volume and flexibility. However, securing portability of the whole detection system needs unconventional effort. Moreover, the non-specific adsorption on the surface of microbeads, pandemic but rarely mentioned, should be effectively prevented, which otherwise seriously deteriorates multiplexed immunoassays. Much simpler readout-control device equipped with powerful functionalities is another prerequisite for suspension array to be more reliable solution for increasing demand of immunosensing.

In this paper, I have proposed an improved immunoassay system employing specially designed gold-virus beads and chip based flow cytometer that provides electric as well as fluorescence signals. Introduction of filamentous virus on PEG-SAM-modified gold layered microspheres leads to substantial advance in the sensitivity of immunoassay. The resistance of PEG-SAM to non-specific adsorption enables multiplex immunoassay of four different human-oriented proteins in undiluted human serum, while the flexible thread-like probes and enlarged surface area owing to the filamentous structure on the beads resulted in enhanced sensitivity.

Combined with the enhanced sensitivity of virus-immobilized bead arrays, the microfluidic DC impedance detection system based on ion current through polyelectrolyte gel plugs greatly reduces the volume of the detection units, necessitating only one optical unit and thereby reinforcing the portability, producibility, and cost-effectiveness. The introduction of size variation and biomimetic materials upon sensor arrays for multiplex immunoassay with fully

operational microfluidic flow cytometer shed a new perspective on IVD tools with genuine point-of-care analysis systems.

# 1.3. Chemically Deposited Cobalt-Based Oxygen-Evolution Electrocatalysts on DOPA-Displaying Filamentous Bacteriophages

## 1.3.1. Introduction

Stimulated by recent issues on environmental pollution and climate change due to fossil fuels, H<sub>2</sub> has emerged as the most promising carbon-neutral energy source. One fascinating strategy for H<sub>2</sub> production is (photo)electrochemical water splitting in which the oxygen evolution reaction (OER) determines the whole cell efficiency as it involves a more complex mechanism than the hydrogen evolution reaction (HER). [34], [35] As non-precious metal based-oxygen evolution catalysts, such as transition metal oxides, become increasingly important, numerous oxygen-evolving catalysts (OECs) including Co-based materials have been tested under relatively benign conditions at low overpotentials. [36]–[38]

Biotemplated nanomaterials are attractive candidates because they provide programmable functional interfaces with well-defined sizes and shapes. A variety of biomaterials, such as bacterial whole cells, flagella, fungi, algae, and viruses, have been introduced for this purpose. [39] In particular, filamentous bacteriophages (phages) have attracted significant attention. [3], [40] Phages are 880 nm in length and 7 nm in width, which comprises replicas of ~2700 major coat proteins (p8) encapsulating single-stranded DNA with minor coat proteins (p7, p9, p6 and p3) anchored at each end of thread-like protein capsid. [2] The coat proteins can be easily modified by genetic engineering, which leads to the customization of structures and surface functionalities of the virus particles. Reportedly, catechol group, well known

for its strong affinity to a broad range of inorganic materials, [21], [41], [42] can be expressed on the major coat protein p8 to act as a strong nucleation center for Au, Ag, Pt, and bimetallic CoPt and FePt. [43]

In this work, I propose catechol groups and tri-glutamates to be introduced onto the major coat proteins of phages to promote the spontaneous deposition of Co-based electrocatalysts. Such 3,4-dihydroxyl-L-phenylalanine DOPA-phages are expected to facilitate Co-oxide precipitation to form  $\text{Co(OH)}_2$ . The Co-based catalysts adhered to DOPA-phages through electroless deposition (Co/DOPA-phages) may have different structures and thus different performance from those of the electrodeposited Co-OEC (Ed-Co). Electrochemical analysis and X-ray photoelectron spectroscopy (XPS) prove the genetically engineered phages to be a superior template for Co-based OER catalysts equipped with distinctive features and assured quality.

## 1.3.2. Experimental

### 1.3.2.1. Materials

BsrG I, BamH I, NEBuffer 3.1, polymerase, dNTP and Gibson assembly reagents were purchased from New England Biolab. TG1 and fd-tet vector received from Lucigen and Invitrogen, respectively. Tetracycline (Bioreagent), Tyrosinase from mushroom, Poly(ethylene glycol) with Mn 8000, NaCl >99.5%, Nitrotetrazolium Blue chloride (NBT) (powder, electrophoresis grade), Glycine 99%, Boric acid 99.5%,  $\text{Co(NO}_3)_2$  99.999%, Nafion 117 (~5% in a mixture of lower aliphatic alcohols and water), and KOH pellets 85% were purchased from Aldrich. 300 kDa size cellulose ester (CE) membrane was from Spectrum Laboratories, Inc.

### 1.3.2.2. Electrochemical Methods

All electrochemical experiments were carried out using CH Instruments 660A and 750A, BASi Pt-wire counter electrode and Ag/AgCl (3 M) reference electrode. Electrode potentials in this work, vs. NHE, were converted from Ag/AgCl (3 M) basis using  $E(\text{NHE}) = E(\text{Ag/AgCl}) + 0.209 \text{ V}$ . Overpotentials were calculated with  $\eta$  (Overpotential) =  $E(\text{NHE}) - (1.23 - 0.0592 \times \text{pH})$ . A GC RDE electrode (0.1963 cm<sup>2</sup>) was polished with 0.3  $\mu\text{m}$  and 0.05  $\mu\text{m}$  alumina powders for 90 s each and sonicated for 30 s with deionized water before every experiment and used as a working electrode unless otherwise stated. All the CVs were acquired after 20 cycles of fast scan (100mV s<sup>-1</sup>) including the region of water oxidation (0.78 V ~ 1.98 V vs. RHE) to stabilize the catalyst

### 1.3.2.3. Fd-tet Phage Engineering.

To introduce TyrGluGluGlu (YE<sub>3</sub>) at the end of the major coat protein of fd-tet, the fd-tet phage vector was cut by BsrG I and BamH I. The inserts were created by polymerase chain reaction (PCR) using primer 1-4. (Table 2) The obtained PCR products were purified and ligated with the vector cut by BsrG I and BamH I using Gibson assembly to yield fd-YE<sub>3</sub>, which was used to transform electrocompetent TG1 and plated on lysogeny broth (LB) containing 20  $\mu\text{g mL}^{-1}$  of tetracycline (tet) for selection. The DNA sequence was verified by DNA sequencing facility of Macrogen Inc. The Tyrosine to DOPA conversion efficiency of 20 colonies was further tested by NBT-Glycine assay. Among those colonies, p8 amino acid sequence of AYE3S which matches to GCGTATGAAGAGGAATCT showed the highest conversion efficiency from tyrosine to DOPA, around 85%. This is the genotype of the DOPA-expressing phages (DOPA-phages) used in this paper.

#### 1.3.2.4. Phages Growth and Purification

TG1 cell containing fd-YE<sub>3</sub> DNA was grown in NZY/tet (20 µg mL<sup>-1</sup>) growth media overnight at 37 °C. E-coli cell was removed from cell culture media via centrifugation at 12,000 g for 10 min. The supernatant was well mixed with 1/5 volume of PEG/NaCl and incubated at 4 °C to be centrifugated at 16,000 g for 20 min next day. The precipitated phages were resuspended with PBS buffer (pH 6.0) and the concentration of phages were verified by spectroscopic method.

#### 1.3.2.5. Tyrosine to DOPA Conversion Efficiency

500 U mL<sup>-1</sup> of tyrosinase was co-incubated with the phages expressing YE<sub>3</sub> (Tyr-phages) overnight at 25 °C and dialyzed using CE membrane of 300 kDa size. One unit will cause an increase in A<sub>280</sub> of 0.001 per minute at pH 6.5 at 25 °C in a 3 mL reaction mix containing L-tyrosine. NBT-Glycine assay was performed to identify the tyrosine to DOPA conversion efficiency based on the previous report. 0.5 mg mL<sup>-1</sup> of NBT in 2 M potassium glycinate buffer (pH 10) was incubated with various dilution of phages containing buffer for 1 h at 25 °C in dark. Absorption was measured at 530 nm and the concentration of DOPA on DOPA-phages was calculated from the absorption of DOPA at 530 nm.

**Table 2. Primers 1-4 used to create inserts.**

Insert 1 (Forward)	Primer 1	5'-CGTATGCGCCTGGTCT-3'
Insert 1 (Reverse)	Primer 2	5'-CTGCAGCGAAAGACAGCATC-3'
Insert 2 (Forward)	Primer 3	5'- CTGTCTTTCGCTGCAGNKTAYGAAGAGG AANNKGATCCCGCAAAGCGGCC-3'
Insert 2 (Reverse)	Primer 4	5'-GGCCTTGATATTCACAAACG-3'



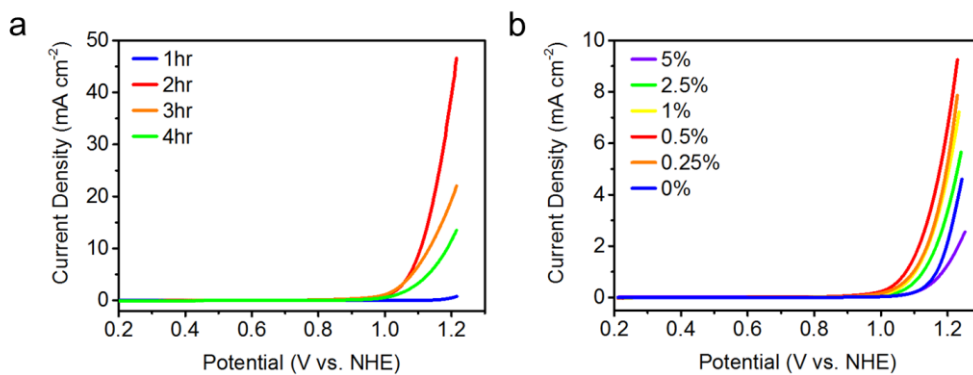


**Fig. 1-9. Optimization of Co/DOPA-phages.**

a. The OER activity of Co/DOPA-phages for a variety of incubation periods for DOPA-phages in the precursor solution. b. The OER activity of Co/DOPA-phages as a function of the amount of nafion solution.

### 1.3.2.7. Electrodeposition of Co-OEC on GC Electrode

Co-OEC Catalyst film was grown on GC RDE in precursor solution (0.5 mM  $\text{Co}(\text{NO}_3)_2$  in 0.1 M  $\text{H}_3\text{BO}_3$  + 50 mM KOH) with controlled potential electrolysis at 1.3 V (vs. NHE) under electrode rotation at 600 rpm. The duration for electrodeposition was 5 min, which the current reached a plateau at  $\sim 4 \text{ mA cm}^{-2}$ .

### 1.3.2.8. Tafel Plot

The data for Tafel plot was collected from  $7 \mu\text{A cm}^{-2}$  to  $1.4 \text{ mA cm}^{-2}$  in logarithmic current density, leading to potential increase of 0.15 V in 0.5 M borate buffer (pH 9.75) with 1 M  $\text{KNO}_3$  as a supporting electrolyte. For current density lower than  $10 \mu\text{A cm}^{-2}$ , the constant current was applied more than 500 s to wait until the potential becomes stable. For current density greater than  $20 \mu\text{A cm}^{-2}$ , it took less than 100 s for the potential to reach the steady state.

### 1.3.2.9. Determination of Faradaic Efficiency

Co/DOPA-phages immobilized  $0.07 \text{ cm}^{-2}$  GC electrode was tightly sealed with paraffin film and deaerated with 99.999%  $\text{N}_2$  for 30 min. The amount of  $\text{O}_2$  before and after each experiment were measured with gas chromatography and subtracted. The peak area of  $\text{O}_2$  was calibrated using 99.999%  $\text{N}_2$  and 99.999%  $\text{O}_2$  as 0% and 100%  $\text{O}_2$ , respectively. As 2 h after sealing passed, the partial pressure of  $\text{O}_2$  without applied potential was measured to be further subtracted from the amount of  $\text{O}_2$  produced from OER. The partial pressure of  $\text{O}_2$  produced under constant overpotential of 0.55 V on Co/DOPA-phages modified GC electrode was determined after 2 h. The volume of the headspace (13.0 mL) and solution (43.0 mL) were measured taking into account of the volume of electrodes and stirring bar. The partial pressure of  $\text{O}_2$  produced under OER was converted using the ideal gas law to yield 19.5  $\mu\text{mol}$  after corrected with  $\text{O}_2$  dissolved in solution using Henry's law. The

charge passed through working electrode (7.95 C) was divided by 4 F to yield Faradaic efficiency of Co/DOPA-phages to 89%.

### 1.3.3. Result and Discussion

The single-stranded DNA of fd-tet is engineered to express tyrosine and tri-glutamates at the N-terminus of the p8 (Tyr-phages). I then treat tyrosinase to convert the expressed tyrosine to DOPA. The DOPA conversion ratio is measured by nitro blue tetrazolium (NBT)/glycine assay. The buffer for tyrosinase reaction is replaced with deionized water using a cellulose ester membrane (300 kDa) to avoid any side reactions. The final concentration of DOPA-phages is optically determined to be  $2.6 \times 10^{11}$  virions  $\text{mL}^{-1}$ . Co-OEC is deposited onto the DOPA-phages by simply immersing the phages in precursor solutions that are normally used for the electrodeposition of Co-OEC in borate buffer (pH 9.2). [36] With the phages in a test tube, Co-OEC begins to precipitate within 1 h (Fig. 1-9). I can observe the formation of sediment on the Tyr-phages in ~4 h of incubation, which can be easily separated from much slower, ~10 h, precipitation without the phages (data not shown). The Pourbaix diagram for cobalt in aqueous solutions shows that  $\text{Co}^{2+}$  ions are more likely to exist as  $\text{Co}(\text{OH})_2$  at ~pH 9. This indicates that the modified surface of DOPA-phages enhances precipitation.

The scanning electron microscopy (SEM) and high-resolution transmission electron microscopy (HRTEM) (Fig. 1-10) images show the overall structure and surface morphology of Co/DOPA-phages. As expected, one-dimensional entangled wires are present along the virus particles. The atomic structure of Co deposited on

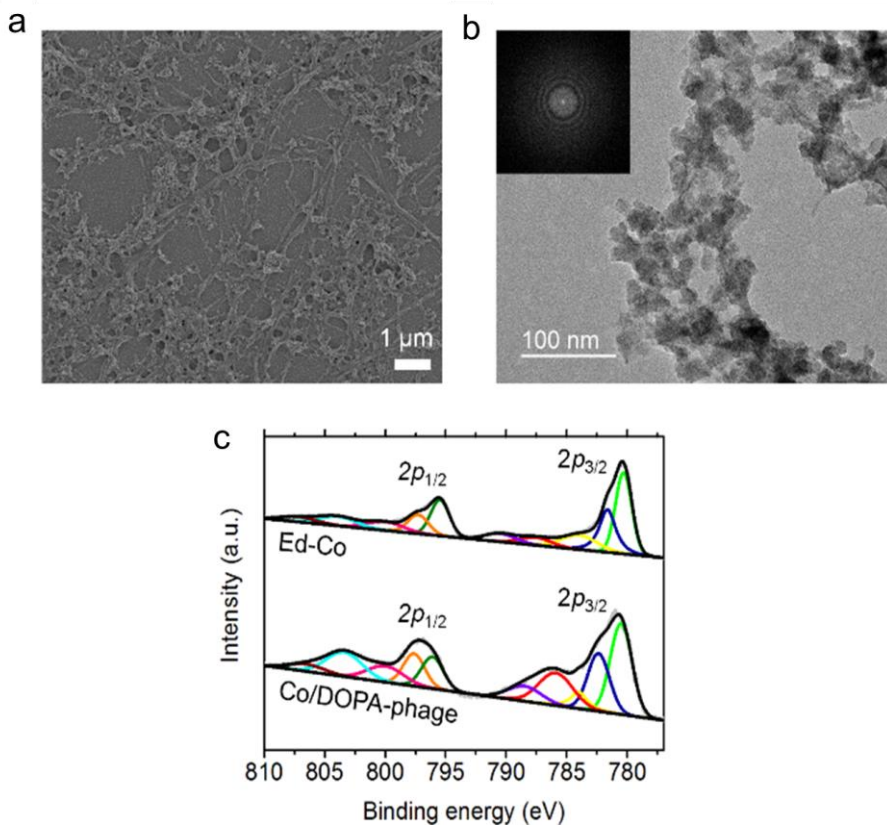


**Fig. 1-10. TEM and SEM images and XP spectra of Co/DOPA-phages.**

a. SEM image of Co/DOPA-phages. b. HRTEM image of Co/DOPA-phages. Inset shows the corresponding FFT pattern. c. Co 2p XP spectra of Ed-Co (upper) and Co/DOPA-phages (lower)

DOPA-displayed phages is amorphous, as shown by the concentric diffraction patterns observed in the fast Fourier transform (FFT) of the HRTEM image (inset in Fig. 1-10 b). Interestingly, the chemical states of cobalt deposited on DOPA-phages analyzed by XPS differ from those of the Ed-Co, which is a widely used Co-based OEC (Fig. 1-10 c). The satellite peak from Co/DOPA-phages at binding energies of Co 2p<sub>3/2</sub> (~786 eV) reveals that most of the cobalt ions are in the divalent state. [44]

To evaluate the OER performance of Co/DOPA-phages, the catalyst ink prepared by mixing Co/DOPA-phages solution and Nafion solution was coated onto the glassy carbon (GC) rotating disk electrode (RDE). Fig. 1-9 presents how the optimal condition for preparing the catalyst ink was determined. All the electrolyte was deaerated with 0.5 M borate buffer (pH 9.75). The full consecutive fast scan cyclic voltammetry shows how as deposited Co/DOPA-phages are stabilized, particularly through the precatalytic wave indicating change in oxidation states of metal cation (Fig. 1-11). The magnified, first 2-cycles of voltammograms are shown in Figure 1-12 a. At the first scan (red curve), two oxidation peaks are observed. The oxidation peak that appears at the lower overpotential vanishes after the first cycle, whereas the position and magnitude of the oxidation peak at the higher overpotential remain unchanged (blue curve). According to the previous literatures, [45] these two peaks can be attributed to the oxidation of Co(OH)<sub>2</sub> to CoOOH and CoOOH to CoO<sub>2</sub>, respectively. The oxidation peak is not found in the cyclic voltammograms for Ed-Co (Fig. 1-13). The Raman spectra in Figure 3b corroborates the fact that Co(OH)<sub>2</sub> on Co/DOPA-phages can be electrochemically oxidized to CoOOH. The A<sub>1g</sub> vibrational mode of CoOOH of the as deposited amorphous Co/DOPA-phages only appears after potential cycling, during which oxygen evolution occurs whereas the peak is shown at as-deposited Ed-Co. [46]

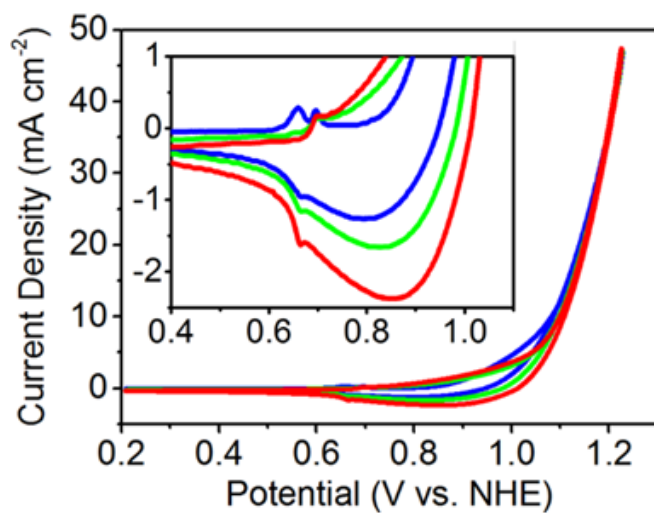


**Fig. 1-11. The 10-cycles of Cyclic voltammograms on GC RDE to stabilize Co/DOPA-phages.**

Scan rate is  $100 \text{ mV s}^{-1}$  under 1600 rpm electrode rotation. The first (blue), the second (green), and the tenth (red) cycles are shown.

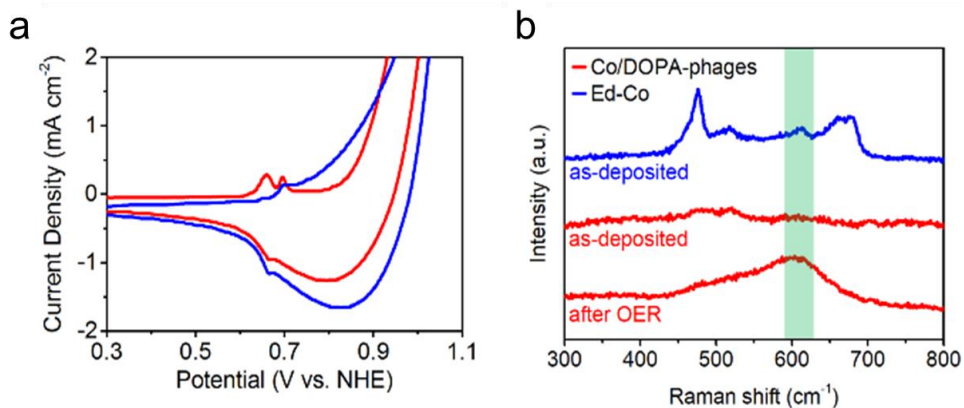


**Fig. 1-12. Consecutive cyclic voltammograms of Co/DOPA-phages and he Raman spectra of Ed-Co and Co/DOPA-phages.**

a. scan rate is  $100 \text{ mV s}^{-1}$  under 1600 rpm electrode rotation. The first (red) and the second (blue) cycles. b. The Raman spectra of as-deposited Ed-Co (blue line) and Co/DOPA-phages (red line) in as-deposited state (upper) and after fast scan including OER region (lower). The peak marked by green bar indicates the A1g vibrational mode originated from CoOOH.

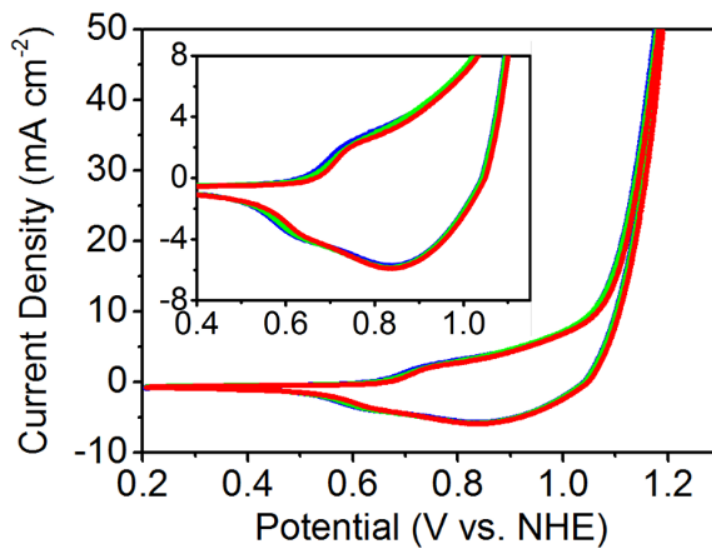


**Fig. 1-13. Consecutive cyclic voltammograms for OER using Ed-Co.**

Consecutive cyclic voltammograms for OER using Ed-Co in deaerated 0.5 M borate buffer at scan rate: 5 mV s<sup>-1</sup> under 1600 rpm electrode rotation (initial curve; blue, 2nd scan; green, 10th scan; red curve).

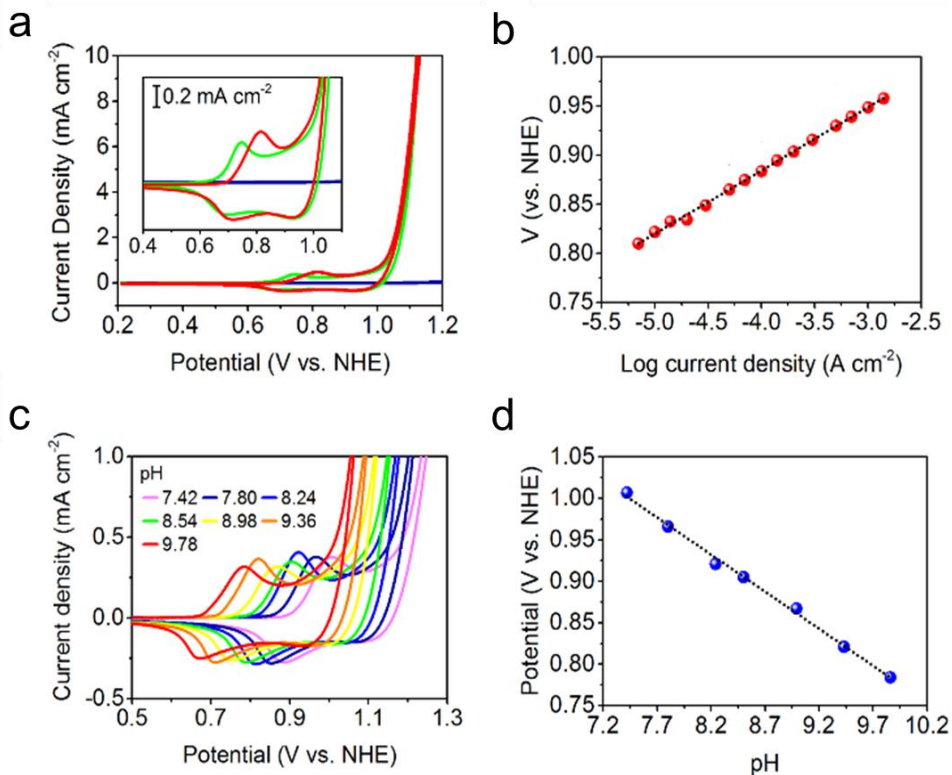


Figure 1-14 shows OER performance of the Co/DOPA-phages deposited on the GC RDE. The voltammograms were obtained after 10 cycles of fast scans. Overall electrochemical behavior of Co/DOPA-phages is similar to that of Ed-Co (Fig. 1-14). This indicates that the  $\text{Co(OH)}_2$  on DOPA-phages was irreversibly converted to comparable states with Ed-Co, as shown in the oxidation peak that appeared at the lower potential of the first CV scan (Fig. 1-12 a), and it follows the identical transition of  $\text{Co}^{3+}$  to  $\text{Co}^{4+}$  as shown in Ed-Co during the water oxidation reaction. Anodic peaks corresponding to  $\text{Co}^{3+/2+}$ , preceding the catalytic current for water oxidation, appear at  $0.815 (\pm 1.0 \times 10^{-2})$  V and  $0.746 (\pm 7.0 \times 10^{-3})$  V (vs. NHE) for Co/DOPA-phages and Ed-Co, respectively. It should be particularly noted that the oxidative peak for  $\text{Co}^{3+/2+}$  at the Co/DOPA-phages-modified electrode is located at a more positive potential (by 69 mV) than that of Ed-Co. This positive peak shift for  $\text{Co}^{2+}$  oxidation is also observed at the DOPA-phage-modified electrode in the aqueous electrolyte containing  $\text{Co}^{2+}$  ions (Fig. 1-15). By comparing the voltammograms using Tyr-phages-modified and bare GC electrode, I can see that the DOPA moieties are involved in the electrochemical conversion of  $\text{Co}^{2+}$  to  $\text{Co}^{3+}$ . In Figure 1-14a and Figure 1-15, the onset and half-wave potential for  $\text{Co}^{2+}$  oxidation on DOPA-phage-modified electrode are more positive than those of a bare GC electrode. The oxidation from  $\text{Co}^{2+}$  to  $\text{Co}^{3+}$  is hindered by DOPA. This is obviously nothing to do with unintentional Fe incorporation, [46] as was verified by the XPS experiments (Fig. 1-16). A kinetic barrier of the insulating proteins is not responsible either. If so, the onset of OER of Co/DOPA-phages should be appeared at more positive potential region compared with Ed-Co, but it was not. This phenomenon supposedly comes from the less positive formal potential of the catechol group of DOPA compared with the  $\text{Co}^{3+/2+}$  couples (1.92 V vs. NHE at pH 0). The voltammograms are well understood by the assumption that no oxidation from  $\text{Co}^{2+}$  to  $\text{Co}^{3+}$  takes place unless the catechols are oxidized. It is highly probable that the

catechols on a phage act as mediators that relay electrons from  $\text{Co}^{2+}$  to the GC electrode.

Co/DOPA-phages bring about subtle catalytic enhancement within OER at the low overpotential region. The cathodic shifts of the waves in cyclic voltammograms were  $13.0 (\pm 7.5)$  mV at  $1 \text{ mA cm}^{-2}$  and  $9.50 (\pm 4.4)$  mV at  $2 \text{ mA cm}^{-2}$ . The DOPA-phages system does not involve any inorganic dopant, that might hinder  $\text{Co}^{2+}$  oxidation kinetics. Nonetheless, the OER responses of Co/DOPA-phages and Ed-Co appear to be similar and their overpotentials for  $10 \text{ mA cm}^{-2}$  are almost same (469 mV and 467 mV, respectively) as shown in the voltammograms (Fig. 1-14a).

The analogous potential shift for the metal cation in the catalyst layer has been often observed in the previous literatures. [47]–[49] The introduction of different kinds of metal cations to the nickel (oxy)hydroxide catalyst changes the oxidative peak potential. For example, introduction of iron and manganese gives rise to positive and negative potential peak shifts for  $\text{Ni}^{3+/2+}$ , respectively. [47] For the Fe-doped NiOOH especially, which is the most-active known OER catalyst in alkaline media, incorporation of Fe suppresses the  $\text{Ni}^{2+}$  oxidation by partial charge transfer, leading to a positive shift in the potential at which  $\text{Ni}^{3+/2+}$  redox occurs. Although the active sites for OER in the NiFe-based catalyst are still controversial, it is widely accepted that a partial charge transfer caused by dopant cations leads to activity enhancement by changing the OER mechanism. [49] In addition, electronegativity differences between the dopant and carbon-based catalyst, which assists the partial-charge transfer, have been considered as an activity descriptor for the oxygen reduction (ORR) and OER. [50] Our report shows that further optimization of the molecular group present in the catalyst support could also affect the OER mechanism and improve the performance.



**Fig. 1-14. Electrochemical activity of Co/DOPA-phages.**

a. Cyclic voltammograms for the OER using Co/DOPA-phages (red), Ed-Co (green)-modified GC RDE, and bare GC (blue) RDE in 0.5 M borate buffer at pH 9.75 (scan rate of  $5 \text{ mV s}^{-1}$  under 1600 rpm electrode rotation). b. Tafel plots for the Co/DOPA-phages-modified GC RDE measured by applying a constant current under electrode rotation at 1600 rpm. c. Cyclic voltammograms for a Co/DOPA-phages-deposited GC electrode (scan rate of  $5 \text{ mV s}^{-1}$ ) in 0.5 M boric acid under quiescent conditions at pH 9.78, 9.36, 8.98, 8.54, 8.24, 7.80, and 7.42 (oxidation peaks from left to right). d. pH dependence of the oxidative peak current density shown in c.

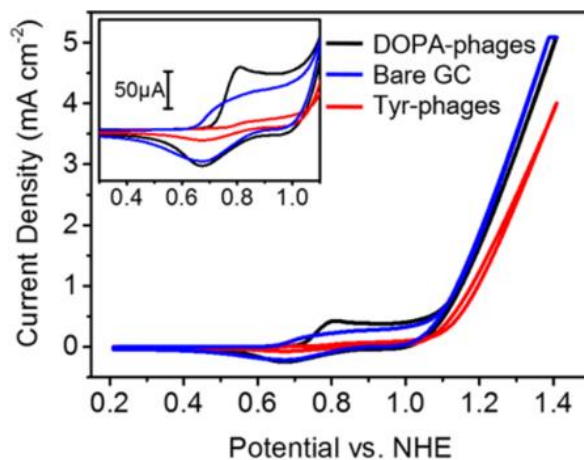


**Fig. 1-15. Electrocatalytic oxidation of  $\text{Co}^{2+}$  ions dissolved in electrolyte on phages-modified and bare GC electrodes.**

The electrode with DOPA-phages gives higher oxidation current for  $\text{Co}^{3+/2+}$  than the bare GC electrode. The Tyr-phages modified electrode barely undergoes electrochemical oxidation for  $\text{Co}^{3+/2+}$ .

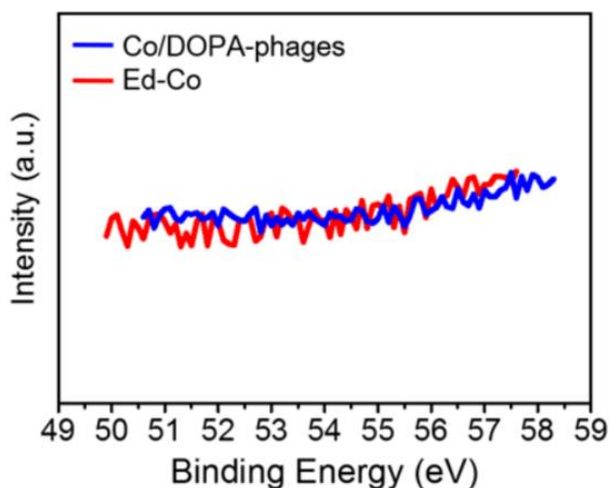


**Fig. 1-16. The binding energies between 50~58 eV in Co/DOPA-phages and Ed-Co.**

The XP spectra ensure that no Fe was incorporated to each catalyst sample. The binding energy region of 3p was investigated instead of 2p to avoid disturbance stemming from the Auger peak of Co which appears in the Fe 2p region.

As shown in Figure 1-14b, the Tafel slope is  $65.3 (\pm 7.6 \times 10^{-2}) \text{ mV dec}^{-1}$  for the Co/DOPA-phages, which is similar to that of other Co-based OECs ( $\sim 59 \text{ mV dec}^{-1}$  corresponds to  $2.3 \times RT F^{-1}$ ). [51] This implies that Co/DOPA-phages catalysts exhibit a reversible one-electron transfer prior to a chemical turnover-limiting step. [51], [52] To elucidate if the oxidation of  $\text{Co}^{2+}$  to  $\text{Co}^{3+}$  involves proton-coupled electron transfer (PCET), I investigated the pH dependence of the preceding anodic peak shown in the cyclic voltammograms for the OER (Fig. 1-14c). Surprisingly, a plot of  $E_{p,a}$  vs. pH reveals a slope of  $89.4 \text{ mV pH}^{-1}$  (Fig. 1-14d), which is in contrast to the value of  $\sim 60 \text{ mV pH}^{-1}$  normally observed for other electrodeposited Co- and Ni-based OECs. [51], [53] The value of  $89.4 \text{ mV pH}^{-1}$  is close to  $90 \text{ mV pH}^{-1}$ , corresponding to the loss of one electron accompanied by the transfer of  $\sim 1.5$  protons. This suggests an operative mechanism involving  $2e^-/3H^+$ , which was previously proposed for the iridium oxide [54] and Ni-borate OECs. [53] Further structural analysis of Co/DOPA-phages during the OER and investigation of in-depth mechanism are underway using in situ spectroscopy techniques (e.g. Raman and X-ray absorption near edge structure).

The faradaic efficiency for gaseous  $\text{O}_2$  generation is 89% (see 1.3.2.9). The heterogeneous film of Co/DOPA-phages retain its stable performance for 2 h under a constant overpotential at 500 mV, showing  $12.37 \text{ mA cm}^{-2}$  that corresponds to 99.6 % of the initial current density (Fig. 1-18a). Under a constant current density of  $10 \text{ mA cm}^{-2}$ , the potential decreases by 0.02% in 2 h (Fig. 1-18b). The stability remains unchanged for 9 h with a 0.23% rise in the potential (Fig. 1-17), whereas the potential

for Ed-Co is stable only for ~3 h. Even though the overpotentials for  $10 \text{ mA cm}^{-2}$  at the initial cyclic voltammograms (Fig. 1-14a) are similar between Co/DOPA-phages and Ed/Co, the overpotential for Co/DOPA-phages is 40 mV lower than that of Ed-Co after the two-hour electrolysis (Fig. 1-17). The abrupt potential rise for both samples is due to detachment of the catalyst film from the RDE surface. The biomaterial, DOPA-phages itself was not oxidized during the water oxidation confirmed by the quantitative phage protein analysis after the OER (Fig. 1-19).

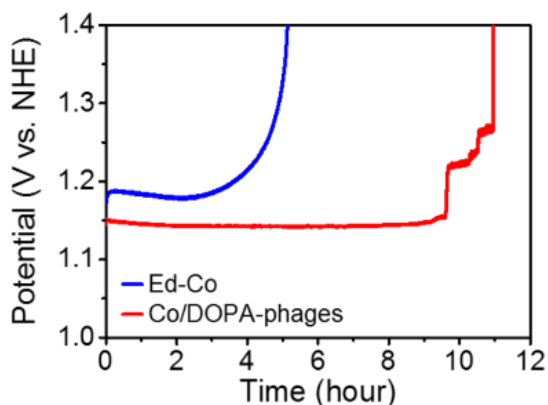


**Fig. 1-17. Durability test of Ed-Co and Co/DOPA-phages.**

Durability test of Ed-Co and Co/DOPA-phages under constant current density of  $10 \text{ mA cm}^{-2}$ . The electrode rotation rate was 1600 rpm and the electrolyte was deaerated 0.5 M borate buffer (pH 9.75).

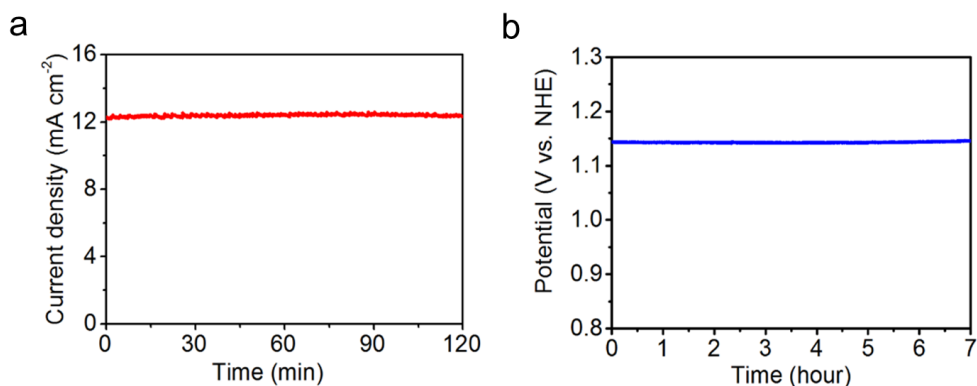


**Fig. 1-18. Stability of Co/DOPA-phages modified RDE.**

a. Two-hour stability probed by the steady-state current density, which was obtained using a Co/DOPA-phages modified RDE held at 1.16 V (vs. NHE), corresponding to 500 mV of overpotential, and b. steady-state potential at  $10 \text{ mA cm}^{-2}$ , respectively. Rotation rate of the electrode was 1600 rpm and the electrolyte was deaerated 0.5 M borate buffer (pH 9.75).

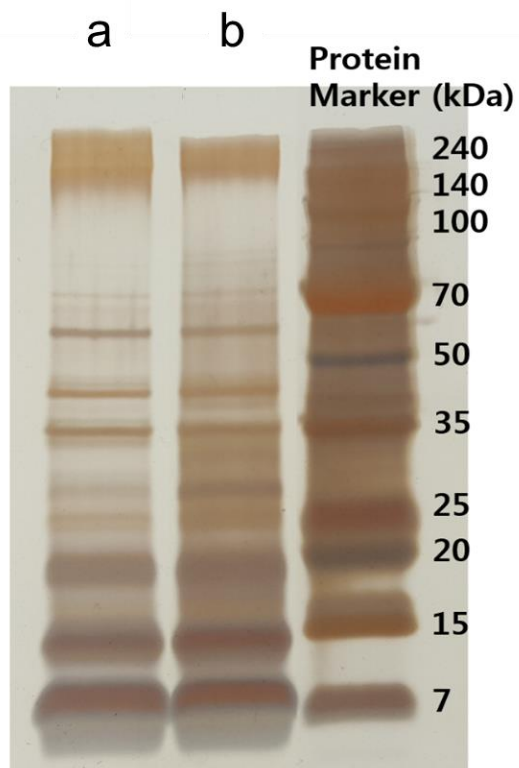


**Fig. 1-19. Stability of phage under OER condition.**

The result of silver staining under a. 1.08 V and b. 1.73 V (vs. RHE). The amounts of p8 major coat protein, which shows typical strong and dragging bands near 7 kDa, are not significantly different from each other.



### 1.3.4. Conclusion

In this study, I incorporated DOPA on the surface of the filamentous bacteriophage on which Co-OEC was spontaneously precipitated. The Co/DOPA-phages catalyst is compatible with mass production in solution phase with assured quality. The catechol group of DOPA appears to serve as a dopant as well as an electron mediator, playing two roles, i.e. stabilization of  $\text{Co}^{2+}$  and slight enhancement of the OER activity in a low overpotential region, probably by lowering the thermodynamic potential of PCET pre-equilibrium. [36] Compared with the previous studies utilizing electroless deposition technique, [21] the proposed Co/DOPA-phages herein provide an unconventional way of creating electrocatalysts at specific molecular moieties for the OER. The prominent OER activity under  $10 \text{ mA cm}^{-2}$  and long-term stability of Co/DOPA-phages suggest potential for further advancement via denser and systematically ordered array of catechol groups and incorporation of secondary conductive supports to enhance the conductivity. Further research effort would unravel diverse functionalities of DOPA for promoting the Co-OEC precipitation, tuning the interactions with metal centers through coordination, and relaying electrons between the OER catalytic site and underlying electrode as a redox mediator.

## 1.4. Genetic engineering of filamentous bacteriophage (fd) for the application in SERS active probe.

### 1.4.1. Introduction

Filamentous bacteriophage has several capsids that are frequently utilized for genetic engineering. Among those capsid, p8 account for the majority of the capsid. However, the phage-displayed library depends on the quality of display, and the level of display for different polypeptides vary greatly, depending on the length and the sequence of peptides. [55], [56] P8 is composed of 50-residue amino acids and can be divided into three compartments. The first 10 residue that are the closest to the single stand DNA of filamentous bacteriophage, they contain lysine groups and interact with the negative charge of DNA. The second 20 residue contains hydrophobic group, and the outmost 20 residue of filamentous bacteriophage is composed of

In this work, random libraries are introduced at the p8 of filamentous bacteriophage for the expression of four foreign protein (one tyrosine and three glutamic acid), and the expression efficiency is analyzed with the number of virions and NBT assay. The sequence from library that produce target foreign protein most efficiency is sequenced, and back transformed to produce target protein reproducibly, and repeatedly. The filamentous bacteriophage with one tyrosine and three glutamic acid is further utilized as a SERS template, which immobilized gold nanoparticles spontaneously on it. The efficiency as a SERS template of phage with YEEE on p8 and wild type was compared with the signal intensity from 4-nitrobenzenethiol.

## 1.4.2. Experimental

### 1.4.2.1. Genetic Engineering of Filamentous Bacteriophage

To introduce TyrGluGluGlu (YEEE) and acceptor peptide at the end of the major coat protein of fd-tet, the fd-tet phage vector was cut by BsrG I and BamH I. The inserts were created by polymerase chain reaction (PCR) using primer 1-4. (Table 3) The obtained PCR products were purified and ligated with the vector cut by BsrG I and BamH I using Gibson assembly, which was used to transform electrocompetent TG1 and plated on lysogeny broth (LB) containing 20  $\mu\text{g mL}^{-1}$  of tetracycline (tet) for selection. The DNA sequence was verified by DNA sequencing facility of Macrogen Inc. The Tyrosine to DOPA conversion efficiency of 20 colonies was further tested by NBT-Glycine assay. Among those colonies, p8 amino acid sequence of AYEEES which matches to GCGTATGAAGAGGAATCT showed the highest conversion efficiency from tyrosine to DOPA, around 85%.

**Table 3. Primer 1-4 for the genetic engineering of filamentous bacteriophage**

Insert 1 (Forward)	Primer 1	5'-CGTATGCGCCTGGTCT-3'
Insert 1 (Reverse)	Primer 2	5'-CTGCAGCGAAAGACAGCATC-3'

Insert 2 (Forward)	Primer 3	5'- GCTGTCTTTTCGCTGCAGNKTAYGAAGAGG AANNKGATCCCGCAAAAGCGGCC-3'
Insert 2 (Reverse)	Primer 4	5'-GGCCTTGATATTCACAAACG-3'

#### 1.4.2.2. Phage Growth and Purification

TG1 cell containing DNA of filamentous bacteriophage was grown in NZY/tet (20 µg mL<sup>-1</sup>) growth media overnight at 37 °C. E-coli cell was removed from cell culture media via centrifugation at 12,000 g for 10 min. The supernatant was well mixed with 1/5 volume of PEG/NaCl and incubated at 4 °C to be centrifugated at 16,000 g for 20 min next day. The precipitated phages were resuspended with PBS buffer (pH 6.0) and the concentration of phages were verified by spectroscopic method.

#### 1.4.2.3. Analyzing the Expression Efficiency with NBT Assay

500 U mL<sup>-1</sup> of tyrosinase was co-incubated with the phages expressing YEEE overnight at 25 °C and dialyzed using CE membrane of 300 kDa size. One unit will cause an increase in A280 of 0.001 per minute at pH 6.5 at 25 °C in a 3 mL reaction mix containing L-tyrosine. NBT-Glycine assay was performed to identify the tyrosine to DOPA conversion efficiency based on the previous report. 0.5 mg mL<sup>-1</sup> of NBT in 2 M potassium glycinate buffer (pH 10) was incubated with various dilution of phages containing buffer for 1 h at 25 °C in dark. Absorption was

measured at 530 nm and the concentration of DOPA on phage was calculated from the absorption at 530 nm

#### 1.4.2.4. Spontaneous Immobilization of Gold Nanoparticles onto Phage and Raman Measurement

$5.5 \times 10^{12}$  gold nanoparticles with 5 nm in diameter are incubated with  $4.3 \times 10^{11}$  phages expressing YEEE on p8. After 5 hours of incubation, the sediments were carefully washed 3 times with DPBS, The sediments were incubated with 5 mM of 4-nitrobenzenethiol (NB) for 1 hour, and Raman spectra were obtained using a homemade Ramboss Micro-Raman system spectrometer equipped with TE cooled (-50 °C) charged-coupled device (CCD) camera ( $1024 \times 128$  pixels). The laser beam was focused on a spot approximately 2  $\mu\text{m}$  in diameter through an objective lens of 100 $\times$  magnification. The grating (1200 grooves  $\text{mm}^{-1}$ ) and the slit provided a spectral resolution of 4  $\text{cm}^{-1}$ . Calibration of the spectrometer was conducted with the Raman band of a silicon wafer at 520  $\text{cm}^{-1}$ . 633 nm He-Ne laser was used with the exposure time of 10 seconds.

### 1.4.3. Result and Discussion

To express 3,4-dihydroxyl-L-phenylalanine (DOPA) on filamentous bacteriophage, YEEE peptide is engineered to be expressed on the N-terminus of p8 peptide of bacteriophage. At the same time, acceptor peptide is expressed on the N-terminus of p3 to further immobilize filamentous bacteriophage on the micro-size bead. For the maximum expression of YEEE on p8 of filamentous bacteriophage, random library is introduced. DNA base triplets of tyrosine is TAT and TAC, so the primer for tyrosine is designed to be TAY. For the DNA base before tyrosine, GNK is encoded to facilitate the expression of tyrosine. After the DNA base triplets of YEEE (TAYGAAGAGGAA), NNK is encoded for easy expression of p8.

The DNA cut and PCR product is analyzed with EtBr gel-electrophoresis (Figure 1-20). The two fragments of PCR inserts with 0.9 kb is generated with primer 1 and 2, and 0.4 kb is generated with primer 3 and 4 (Table 2). Figure 1-20 (b) shows the PCR product from primer 3 and 4, with the concentration of 85.2 ng/ $\mu$ l, 42.3 ng/ $\mu$ l, and 46.8 ng/ $\mu$ l. Figure 1-20 (c) shows the PCR product from primer 1 and 2, with 147.0 ng/ $\mu$ l in concentration. Figure 1-20 (a) is the result of DNA cut with BsrG1 and BamH1, with the concentration of 26.8 ng/ $\mu$ l, 29.4 ng/ $\mu$ l, and 10 ng/ $\mu$ l. The three compartment Gibson assembly with these three fragments (figure 1-20 (a), (b), and (c)) was failed, and the Gibson assembly was tried again with the freshly prepped, higher concentration of DNA cut (Figure 1-21). The concentration of DNA cuts in figure 1-21 (c) is 24.5 ng/ $\mu$ l for each well, which shows much brighter band from EtBr gel electrophoresis, which means better quality of DNA cut. Figure 1-21 (a) is 27 ng/ $\mu$ l and Figure 1-21 (b) is 12.5 ng/ $\mu$ l. The three compartment Gibson assembly was successfully conducted with these three DNA fragments (1-21 (a), (b), and (c)), and the product was sequenced to confirm the insert of random sequences. Figure 1-22 shows the result of sequencing, and N, K, Y, N, N, and K is successfully encoded

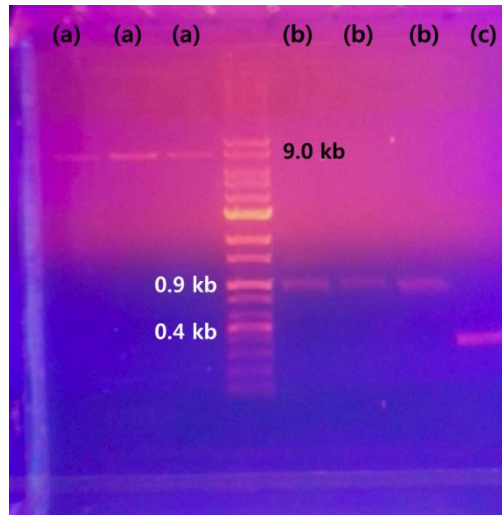


**Fig. 1-20.** The PCR products and DNA cuts are analyzed with EtBr gel-electrophoresis.

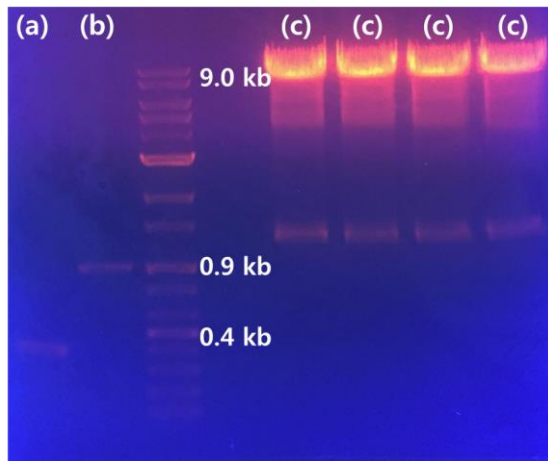


**Fig. 1-21.** The PCR products and DNA cuts are analyzed with EtBr gel-electrophoresis. The higher concentration of template DNA result in brighter bands.

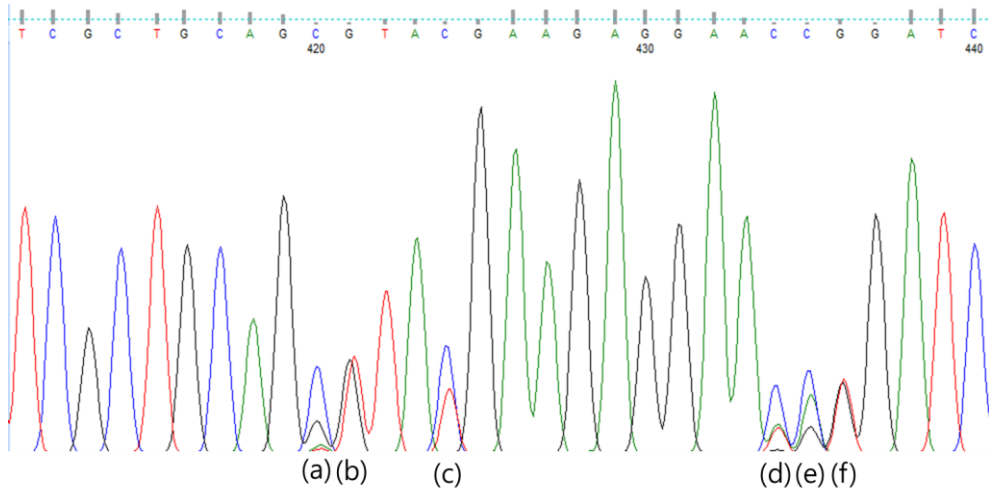


**Fig. 1-22. The result of sequencing of DNA with random sequences.**



at 1-22 (a), (b), (c), (d), (e) and (f), respectively. After the inserts are confirmed, the filamentous bacteriophage with those random sequences are produced and purified.

The number of produced and purified filamentous bacteriophages are analyzed with UV-visible spectrophotometer. The purified filamentous bacteriophages are known to show its maximum absorbance at 269 nm, but the filamentous bacteriophages before centrifugation showed broad and ambiguous peak around ~270 nm (figure 1-23 (a)). After the purified phages are centrifugated at 13,000 rpm for 30 seconds, the supernatants are analyzed with UV-visible spectrophotometer, which showed relatively clear peak around ~270 nm (figure 1-23 (b)). The number of phages were decreased 1.4 % before and after centrifugation. I suppose the cell debris from bacteria cell culture media is removed by centrifugation.

To analyze the YEEE expression efficiency on p8, randomly picked 10 different colonies from library transformation were sequenced. As it is shown from table 4, except colony #4, 9 colonies are confirmed to be successfully encoding random sequences before and after YEEE. Except colony #4, the phage production efficiency and tyrosine expression efficiency are analyzed with NBT/glycine assay. Among the 9 colonies, colony #2 (GCGTATGAAGAGGAATCT) showed the highest phage production efficiency and tyrosine expression, which were 85 %, was used for the genotype of YEEE phage. To analyze the acceptor peptides expressed on p3, phages are first western blotted and then transferred to be analyzed with streptavidin-horseradish peroxidase (streptavidin-HRP). Figure 1-24 shows the result, with (a) and (b) shows streptavidin-HRP signal from phages from colony #1 and #2 (from

table 4), respectively. The HRP signal is clearly observed for both (a) and (b), at the protein size near ~70 kDa, which matches well with the sum of molecular weight of p3 protein and acceptor peptide. Phages from colony #2 (Figure 1-24(b)) shows higher concentration of acceptor peptide expressed onto p3 protein, which matches well with the phage production efficiency analyzed with UV-visible spectrophotometer and NBT/glycine assay.

Gold nanoparticles with 5 nm in diameter are immobilized on the surface of p8 protein, which further utilized as a SERS active probes. As it was shown from figure 1-25, phages with YEEE expressed on the p8 shows higher Raman intensity compared to the wild type phages, which is probably due to the facile immobilization of gold nanoparticles on p8 taking advantage of the electrostatic interaction between gold and glutamic acids.

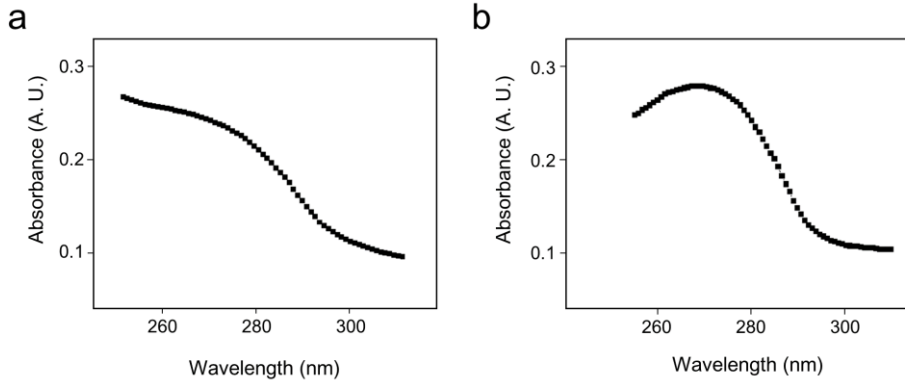


**Fig. 1-23. The absorption spectrum of filamentous bacteriophage (a) before and (b) after centrifugation.**

**Table 4. The result of sequencing of 10 randomly picked colonies of filamentous bacteriophage.**

# of random colony	GNK	TAY (Y)	NNK
1	GCT (A)	TAT	TCG (S)
2	GCG (A)	TAT	TCT (S)
3	GCT (A)	TAC	AAG (K)
4	- (Wild type)	-	-
5	GCT (A)	TAT	TCG (S)
6	GTT (V)	TAC	AGT (S)
7	GTG (V)	TAC	GCT (A)
8	GCG (A)	TAC	GCT (A)
9	GTT (V)	TAC	CCG (P)
10	GGG (G)	TAC	ACG (T)

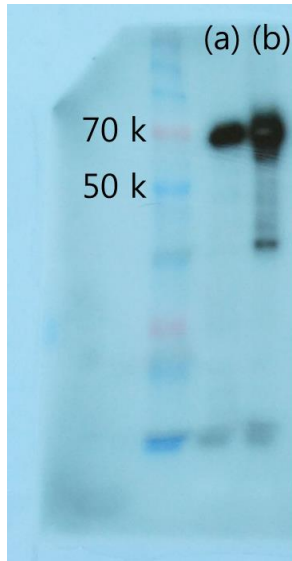


**Fig. 1-24. Acceptor peptide expressed at p3 is verified with western blot.**

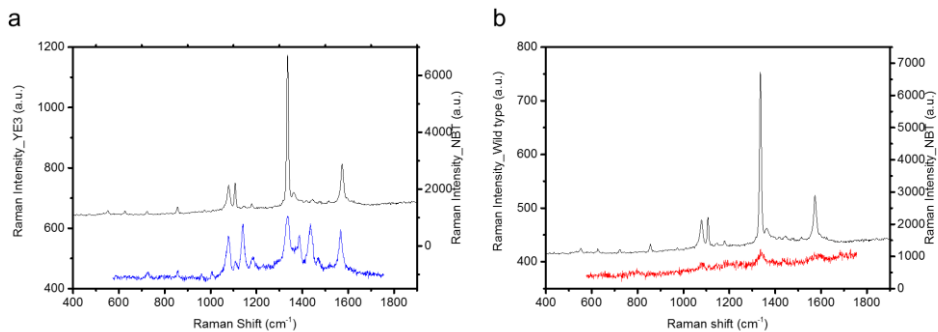


**Fig. 1-25. The Raman shift from (a) genetically engineered phage and (b) wild type phage.**

Raman shift from NB conjugated gold nanoparticles immobilized on the genetically engineered phages ((a), blue), wild type phages ((b), red), and NB on gold wafer (black).

#### 1.4.4. Conclusion

In this work, filamentous bacteriophage (fd) is genetically engineered to express YEEE on p8, and acceptor peptide on p3. To facilitate the production of filamentous bacteriophage, random libraries are introduced before and after YEEE sequence on p8. DNA base triplet GNK is introduced before tyrosine, which also includes random sequence, TAY, to maximize the effective production of filamentous bacteriophage. DNA base triplet of NNK is introduced after glutamic acids. DNA base triplets of GCGTATGAAGAGGAATCT, which can be translated into AYEEES is determined to be shown the optimum expression of YEEE on p8 of filamentous bacteriophage. Three compartment Gibson assembly was tried with various concentration and quality of DNA. The quality and the concentration of cut DNA seems important for the ligation of DNAs into target vector, along with careful purification process. The genetically engineered filamentous bacteriophages were produced and purified. The as-produced phages seem to contain protein debris from bacteria cell culture media, which may be separated with short centrifugation process. The number of phage virions before and after the centrifugation process shows little decrease, as it was analyzed with UV-visible spectrophotometer. The filamentous bacteriophage with one tyrosine and three glutamic acid is further utilized as a SERS template, which immobilized gold nanoparticles spontaneously on it. The efficiency as a SERS template of phage with YEEE on p8 and wild type was compared with the signal intensity from 4-nitrobenzenethiol.

## 1.5. References

- [1] D. A. Marvin, L. C. Welsh, M. F. Symmons, W. R. P. Scott, and S. K. Straus, "Molecular structure of fd (f1, M13) filamentous bacteriophage refined with respect to X-ray fibre diffraction and solid-state NMR data supports specific models of phage assembly at the bacterial membrane," *J. Mol. Biol.*, vol. 355, no. 2, pp. 294–309, 2006.
- [2] Y. A. Wang, X. Yu, S. Overman, M. Tsuboi, G. J. Thomas, and E. H. Egelman, "The Structure of a Filamentous Bacteriophage," *J. Mol. Biol.*, vol. 361, no. 2, pp. 209–215, 2006.
- [3] K. T. Nam *et al.*, "Virus-enabled synthesis and assembly of nanowires for lithium ion battery electrodes.," *Science*, vol. 312, no. 5775, pp. 885–8, May 2006.
- [4] W. C. Records, Y. Yoon, J. F. Ohmura, N. Chanut, and A. M. Belcher, "Virus-templated Pt–Ni(OH)<sub>2</sub> nanonetworks for enhanced electrocatalytic reduction of water," *Nano Energy*, vol. 58, pp. 167–174, Apr. 2019.
- [5] C. K. Jeong *et al.*, "Virus-Directed Design of a Flexible BaTiO<sub>3</sub> Nanogenerator," *ACS Nano*, vol. 7, no. 12, pp. 11016–11025, Dec. 2013.
- [6] J. Wang, L. Wang, X. Li, and C. Mao, "Virus activated artificial ECM induces the osteoblastic differentiation of mesenchymal stem cells without osteogenic supplements," *Sci. Rep.*, vol. 3, no. 1, p. 1242, Dec. 2013.
- [7] J. Wang, M. Yang, Y. Zhu, L. Wang, A. P. Tomsia, and C. Mao, "Phage Nanofibers Induce Vascularized Osteogenesis in 3D Printed Bone Scaffolds," *Adv. Mater.*, vol. 26, no. 29, pp. 4961–4966, Aug. 2014.
- [8] W. J. Chung, D. Y. Lee, and S. Y. Yoo, "Chemical modulation of m13 bacteriophage and its functional opportunities for nanomedicine," *Int. J. Nanomedicine*, vol. 9, no. 1, pp. 5825–5836, 2014.
- [9] R. A. Blaik, E. Lan, Y. Huang, and B. Dunn, "Gold-Coated M13 Bacteriophage as a Template for Glucose Oxidase Biofuel Cells with Direct Electron Transfer," *ACS Nano*, vol. 10, no. 1, pp. 324–332, Jan. 2016.
- [10] L. Han, C. Shao, B. Liang, and A. Liu, "Genetically Engineered Phage-Templated MnO<sub>2</sub> Nanowires: Synthesis and Their Application in Electrochemical Glucose Biosensor Operated at Neutral pH Condition," *ACS Appl. Mater. Interfaces*, vol. 8, no. 22, pp. 13768–13776, Jun. 2016.
- [11] A. Bhasin *et al.*, "The Virus Bioresistor: Wiring Virus Particles for the Direct, Label-Free Detection of Target Proteins," *Nano Lett.*, vol. 18, no. 6, pp. 3623–3629, Jun. 2018.

- [12] S. Niyomdechana *et al.*, “Phage-based capacitive biosensor for Salmonella detection,” *Talanta*, vol. 188, pp. 658–664, Oct. 2018.
- [13] A. F. Ogata *et al.*, “Virus-Enabled Biosensor for Human Serum Albumin,” *Anal. Chem.*, vol. 89, no. 2, pp. 1373–1381, Jan. 2017.
- [14] M. Janczuk-Richter, I. Marinović, J. Niedziółka-Jönsson, and K. Szot-Karpińska, “Recent applications of bacteriophage-based electrodes: A mini-review,” *Electrochem. commun.*, vol. 99, pp. 11–15, Feb. 2019.
- [15] J. Wang, “Electrochemical biosensors: Towards point-of-care cancer diagnostics,” *Biosens. Bioelectron.*, vol. 21, no. 10, pp. 1887–1892, Apr. 2006.
- [16] S. Sharma, J. Zapatero-Rodríguez, P. Estrela, and R. O’Kennedy, “Point-of-Care Diagnostics in Low Resource Settings: Present Status and Future Role of Microfluidics,” *Biosensors*, vol. 5, no. 3, pp. 577–601, Aug. 2015.
- [17] V. Silin, H. Weetall, and D. J. Vanderah, “SPR Studies of the Nonspecific Adsorption Kinetics of Human IgG and BSA on Gold Surfaces Modified by Self-Assembled Monolayers (SAMs),” *J. Colloid Interface Sci.*, vol. 185, no. 1, pp. 94–103, Jan. 1997.
- [18] C. Siegers, M. Biesalski, and R. Haag, “Self-Assembled Monolayers of Dendritic Polyglycerol Derivatives on Gold That Resist the Adsorption of Proteins,” *Chem. - A Eur. J.*, vol. 10, no. 11, pp. 2831–2838, Jun. 2004.
- [19] M. Heuberger, T. Drobek, and J. Vörös, “About the Role of Water in Surface-Grafted Poly(ethylene glycol) Layers,” *Langmuir*, vol. 20, no. 22, pp. 9445–9448, Oct. 2004.
- [20] D. Holmes, J. K. She, P. L. Roach, and H. Morgan, “Bead-based immunoassays using a micro-chip flow cytometer,” *Lab Chip*, vol. 7, no. 8, pp. 1048–1056, Aug. 2007.
- [21] S. R. Quake, A. Y. Fu, C. Spence, A. Scherer, and F. H. Arnold, “A microfabricated fluorescence-activated cell sorter,” *Nat. Biotechnol.*, vol. 17, no. 11, pp. 1109–1111, Nov. 1999.
- [22] C. Wyatt Shields IV, C. D. Reyes, and G. P. Lopez, “Microfluidic cell sorting: a review of the advances in the separation of cells from debulking to rare cell isolation,” *Lab Chip*, vol. 15, no. 5, pp. 1230–1249, 2015.
- [23] H. Choi *et al.*, “A flow cytometry-based submicron-sized bacterial detection system using a movable virtual wall,” *Lab Chip*, vol. 14, no. 13, pp. 2327–33, 2014.



- [24] S. Joo, K. H. Kim, H. C. Kim, and T. D. Chung, "A portable microfluidic flow cytometer based on simultaneous detection of impedance and fluorescence," *Biosens. Bioelectron.*, vol. 25, no. 6, pp. 1509–1515, 2010.
- [25] H. Choi *et al.*, "A label-free DC impedance-based microcytometer for circulating rare cancer cell counting," *Lab Chip*, vol. 13, no. 5, p. 970, Feb. 2013.
- [26] C. S. Jeon, I. Hwang, and T. D. Chung, "Virus-tethered magnetic gold microspheres with biomimetic architectures for enhanced immunoassays," *Adv. Funct. Mater.*, vol. 23, no. 12, pp. 1484–1489, 2013.
- [27] E. J. Kim, C. S. Jeon, I. Hwang, and T. D. Chung, "Translocation Pathway-Dependent Assembly of Streptavidin- and Antibody-Binding Filamentous Virus-Like Particles," *Small*, vol. 13, no. 5, p. 1601693, Feb. 2017.
- [28] H. Seitz and S. Schumacher, *Molecular Diagnostics*. Springer Berlin Heidelberg, 2014.
- [29] J. Park *et al.*, "Asymmetric nozzle structure for particles converging into a highly confined region," *Curr. Appl. Phys.*, vol. 6, no. 6 SPEC. ISS., pp. 992–995, 2006.
- [30] H. Yun, K. Kim, and W. G. Lee, "Effect of a dual inlet channel on cell loading in microfluidics," *Biomicrofluidics*, vol. 8, no. 6, 2014.
- [31] H. J. de Haard *et al.*, "A large non-immunized human Fab fragment phage library that permits rapid isolation and kinetic analysis of high affinity antibodies," *J. Biol. Chem.*, vol. 274, no. 26, pp. 18218–30, Jun. 1999.
- [32] R. M. T. de Wildt, C. R. Mundy, B. D. Gorick, and I. M. Tomlinson, "Antibody arrays for high-throughput screening of antibody-antigen interactions," *Nat Biotech*, vol. 18, no. 9, pp. 989–994, Sep. 2000.
- [33] S.-R. Kwon, C. S. Jeon, N. Y. Hong, K. P. Kim, I. Hwang, and T. D. Chung, "Gold-plated magnetic polymers for highly specific enrichment and label-free detection of blood biomarkers under physiological conditions," *Chem. Commun.*, vol. 50, no. 70, pp. 10066–10069, Aug. 2014.
- [34] K. Jin *et al.*, "Hydrated Manganese(II) Phosphate ( $\text{Mn}_3(\text{PO}_4)_2 \cdot 3\text{H}_2\text{O}$ ) as a Water Oxidation Catalyst," *J. Am. Chem. Soc.*, vol. 136, no. 20, pp. 7435–7443, May 2014.
- [35] L. C. Seitz *et al.*, "A highly active and stable  $\text{IrO}_x/\text{SrIrO}_3$  catalyst for the oxygen evolution reaction," *Science*, vol. 353, no. 6303, pp. 1011–1014, Sep. 2016.

- [36] Y. Surendranath, M. Dincă, and D. G. Nocera, "Electrolyte-Dependent Electrosynthesis and Activity of Cobalt-Based Water Oxidation Catalysts," *J. Am. Chem. Soc.*, vol. 131, no. 7, pp. 2615–2620, Feb. 2009.
- [37] D. K. Bediako, C. Costentin, E. C. Jones, D. G. Nocera, and J.-M. Savéant, "Proton–Electron Transport and Transfer in Electrocatalytic Films. Application to a Cobalt-Based O<sub>2</sub>-Evolution Catalyst," *J. Am. Chem. Soc.*, vol. 135, no. 28, pp. 10492–10502, Jul. 2013.
- [38] C. C. L. McCrory, S. Jung, J. C. Peters, and T. F. Jaramillo, "Benchmarking Heterogeneous Electrocatalysts for the Oxygen Evolution Reaction," *J. Am. Chem. Soc.*, vol. 135, no. 45, pp. 16977–16987, Nov. 2013.
- [39] R. Selvakumar, N. Seethalakshmi, P. Thavamani, R. Naidu, and M. Megharaj, "Recent advances in the synthesis of inorganic nano/microstructures using microbial biotemplates and their applications," *RSC Adv.*, vol. 4, no. 94, pp. 52156–52169, Oct. 2014.
- [40] Y. S. Nam *et al.*, "Biologically templated photocatalytic nanostructures for sustained light-driven water oxidation," *Nat. Nanotechnol.*, vol. 5, no. 5, pp. 340–344, May 2010.
- [41] Y. Liu, K. Ai, and L. Lu, "Polydopamine and Its Derivative Materials: Synthesis and Promising Applications in Energy, Environmental, and Biomedical Fields," *Chem. Rev.*, vol. 114, no. 9, pp. 5057–5115, May 2014.
- [42] S. Y. Lee, S. Y. Lim, D. Seo, J.-Y. Lee, and T. D. Chung, "Light-Driven Highly Selective Conversion of CO<sub>2</sub> to Formate by Electrosynthesized Enzyme/Cofactor Thin Film Electrode," *Adv. Energy Mater.*, vol. 6, no. 11, p. 1502207, Jun. 2016.
- [43] J. P. Park, M. Do, H.-E. Jin, S.-W. Lee, and H. Lee, "M13 Bacteriophage Displaying DOPA on Surfaces: Fabrication of Various Nanostructured Inorganic Materials without Time-Consuming Screening Processes," *ACS Appl. Mater. Interfaces*, vol. 6, no. 21, pp. 18653–18660, Nov. 2014.
- [44] F. Song and X. Hu, "Ultrathin Cobalt–Manganese Layered Double Hydroxide Is an Efficient Oxygen Evolution Catalyst," *J. Am. Chem. Soc.*, vol. 136, no. 47, pp. 16481–16484, Nov. 2014.
- [45] Y.-C. Liu, J. A. Koza, and J. A. Switzer, "Conversion of electrodeposited Co(OH)<sub>2</sub> to CoOOH and Co<sub>3</sub>O<sub>4</sub>, and comparison of their catalytic activity for the oxygen evolution reaction," *Electrochim. Acta*, vol. 140, pp. 359–365, Sep. 2014.
- [46] J. A. Koza, C. M. Hull, Y.-C. Liu, and J. A. Switzer, "Deposition of β-Co(OH)<sub>2</sub> Films by Electrochemical Reduction of

- Tris(ethylenediamine)cobalt(III) in Alkaline Solution,” *Chem. Mater.*, vol. 25, no. 9, pp. 1922–1926, May 2013.
- [47] L. J. Enman, M. S. Burke, A. S. Batchellor, and S. W. Boettcher, “Effects of Intentionally Incorporated Metal Cations on the Oxygen Evolution Electrocatalytic Activity of Nickel (Oxy)hydroxide in Alkaline Media,” *ACS Catal.*, vol. 6, no. 4, pp. 2416–2423, Apr. 2016.
- [48] M. W. Louie and A. T. Bell, “An Investigation of Thin-Film Ni–Fe Oxide Catalysts for the Electrochemical Evolution of Oxygen,” *J. Am. Chem. Soc.*, vol. 135, no. 33, pp. 12329–12337, Aug. 2013.
- [49] L. Trotochaud, S. L. Young, J. K. Ranney, and S. W. Boettcher, “Nickel–Iron Oxyhydroxide Oxygen-Evolution Electrocatalysts: The Role of Intentional and Incidental Iron Incorporation,” *J. Am. Chem. Soc.*, vol. 136, no. 18, pp. 6744–6753, May 2014.
- [50] Z. Zhao, M. Li, L. Zhang, L. Dai, and Z. Xia, “Design Principles for Heteroatom-Doped Carbon Nanomaterials as Highly Efficient Catalysts for Fuel Cells and Metal-Air Batteries,” *Adv. Mater.*, vol. 27, no. 43, pp. 6834–6840, Nov. 2015.
- [51] Y. Surendranath, M. W. Kanan, and D. G. Nocera, “Mechanistic Studies of the Oxygen Evolution Reaction by a Cobalt-Phosphate Catalyst at Neutral pH,” *J. Am. Chem. Soc.*, vol. 132, no. 46, pp. 16501–16509, Nov. 2010.
- [52] Y. Surendranath, D. A. Lutterman, Y. Liu, and D. G. Nocera, “Nucleation, Growth, and Repair of a Cobalt-Based Oxygen Evolving Catalyst,” *J. Am. Chem. Soc.*, vol. 134, no. 14, pp. 6326–6336, Apr. 2012.
- [53] M. Dincă, Y. Surendranath, and D. G. Nocera, “Nickel-borate oxygen-evolving catalyst that functions under benign conditions,” *Proc. Natl. Acad. Sci. U. S. A.*, vol. 107, no. 23, pp. 10337–41, Jun. 2010.
- [54] L. D. Burke and D. P. Whelan, “A voltammetric investigation of the charge storage reactions of hydrous iridium oxide layers,” *J. Electroanal. Chem. Interfacial Electrochem.*, vol. 162, no. 1–2, pp. 121–141, Mar. 1984.
- [55] S. S. Sidhu, “Engineering M13 for phage display,” 2001.
- [56] D. R. Wilson and B. B. Finlay, “Phage display: applications, innovations, and issues in phage and host biology,” *Can. J. Microbiol.*, vol. 44, no. 4, pp. 313–329, Apr. 1998.

# Chapter 2. Development of Sensitivity-Tunable Ion Sensing Platform based on Reverse Electrodialysis

## 2.1. Introduction

Reverse electrodialysis (RED) was first developed in 1954 as a power generation system, where the voltage output is proportional to the ionic concentration difference between sea water and river water. [57] However, earlier versions of REDs fail to serve as an independent power source, for their low power densities. [58] Therefore, for the last decades, trials to augment their power densities have been continued and achieved a meaningful degree of success. A number of publications reported optimizations of constituents [59]–[63] including membranes and spacers, or conditions [64]–[68] including flow rates, operating temperatures and solution concentrations. Recently, REDs were reported to possibly make considerable contribution to biofuel cells, [69] osmosis systems, [70] and photoelectrochemical cells, [71] leading to hybrid power generators in which biocompatible and eco-friendly extra voltage source assists. It was followed by miniaturization of REDs, which was applied to a transdermal drug delivery system [72] and fully ionic circuits for logic processing. [73], [74]

Inspired by cumulative voltage exclusively sensitive to specific ion owing to stack of ion-selective membrane, here I propose a potentiometric ion sensing platform based on RED, which is called multilayer ion-selective membranes (MISM). MISM is composed of ion-selective membrane, where relevant ionophore embedded on membrane gives ion selectivity, and dialysis membrane (DM) which allows electrical and ionic conductivity between the reference and sample solutions. It operates in a simple way that output voltage increases in proportion to the number of membranes constituting the RED. That is a facile method to augment sensitivity that could

exceed the one expected from conventional potentiometric sensors relying on single ion-selective membranes, ideally the Nernst slope. Its sensitivity is tunable by means of the number of membranes for MISM. In this new strategy, MISM does not only act as an ion-selective sensing unit but also as a power source. It produces voltage that contains the information of ion concentration, and also current to operate the system for signal version. The power from a miniaturized MISM is enough to drive data presenting system without any external power source including battery.

Integrating itself with colorimetric apparatus based on bipolar electrode (BPE), MISM successfully transduces voltage signal to color change. Faradaic reactions occur at the two poles of the BPE in an electrolyte channel along which an external potential is applied. [75]–[77] No direct ohmic contact exists between BPE and MISM in the proposed system requiring neither electronics nor battery. Electrochromic dye on BPE can make it possible that ion-selective voltage from MISM come to an end with colorimetric signal readout. Polyaniline (PANi) in this work, which creates continuous gradient of four colors as a function of the applied potential, [78] enables direct quantification of ion concentration with the naked eye. The resulting self-powered data reporting system meets the key conditions for portable, disposable, and easy to use for convenient on-site analysis. I rediscover RED as a tunable ion sensing platform and purely ionic power source to suggest MISM. In combination with appropriate transducers for multicolor readout, MISM leads to an ultimate ion sensing system.

## 2.2. Experimental

### 2.2.1. Membrane fabrication

For NSM, AEMs stored in deionized water were dried completely (at least 15 min), and cut into 1.5 cm × 1.5 cm or 3 cm × 6 cm. The PVC membrane was prepared by mixing thoroughly 5.2 mg of nitrate ionophore, 47.0 mg of dibutyl phthalate, 0.3 mg

of tetraoctylammonium chloride and 47.2 mg of high molecular weight PVC in 5 ml of tetrahydrofuran (THF). The solvent was transferred into a glass petri dish of 4 cm in diameter, and evaporated until an oily mixture was obtained. AEM was dipped into the oily mixture for 5 s so that semi-transparent membrane is formed. After drying for 1 min RT, the obtained NSMs were stored at 4 °C in 10 mM NaNO<sub>3</sub> solution.

For CSM, The CSM was fabricated as follows. The membranes consist of 4.0 mg of calcium ionophore (IV), 2.0 mg of sodium tetraphenylborate, 62 mg of 2-nitrophenyl octyl ether, and 32 mg of PVC high molecular weight dissolved in 5 ml THF. CEMs stored in deionized water were dried for 15 min and cut to 1.5 cm × 1.5 cm. The mixed solution was coated on CEMs in the same manner as the NSM. The obtained CSMs were stored at 4 °C in 10 mM CaCl<sub>2</sub> solution.

DMs were stored in deionized water for nitrate calibration, and in 0.1 M NaNO<sub>3</sub> solution for colorimetric sensor. Before assembling MISM, DMs were cut to 1.5 cm × 1.5 cm and 3 cm × 6 cm and dried for 10 min.

### 2.2.2. MISM assembly

For nitrate calibration and sensitivity tests, I utilized U-shaped spacers by cutting off a 1 cm × 1 cm portion from a 1.5 cm × 2 cm square-shaped rubber. The spacers separate the NSM and DM and act as a solvent chambers for operation. Each stack of MISM is prepared by alternative stacking DMs and NSMs of size 1.5 cm × 1.5 cm between which the spacers are present. Plastic plates were added to the two ends to prop the structure. The reference electrolyte and the analyte solution was alternatively added to each chamber. To the first and the last chambers, an additional 1 mM NaCl was added to define the interfacial potential between the reference electrolyte and the Ag/AgCl electrode. Before the first measurement, MISM was

conditioned by voltage measurement with mixture of 10 mM NaNO<sub>3</sub> and 1 mM NaCl solution.

For the colorimetric sensor, the MISM were prepared following a similar method, but using 3 cm × 6 cm membranes and 2.5 cm × 5.0 cm spacers.

### 2.2.3. Potential measurement

Stacked MISMs is prepared following the above procedure. The detailed conditions such as the type of membrane, the number of stacks, and the type of solution constituting MISM are set according to the purpose of potential measurement, and are mentioned in the main text. Two Ag/AgCl electrodes were respectively put into the two chambers at the extremities of MISM. After addition of the solution to the MISM, voltage of the MISM is measured for 30 s using a potentiostat.

### 2.2.4. Selectivity

The selectivity coefficients were calculated from equation (1).

$$K_{NO_3^-,B}^{pot} = \frac{\Delta\alpha_{NO_3^-}}{\alpha_B} \quad (1)$$

HCO<sub>3</sub><sup>-</sup>, SO<sub>4</sub><sup>2-</sup>, and Cl<sup>-</sup> were selected as the interfering ions (β) and single stack MISM was used for selectivity measurements. The two end chambers were filled with reference electrolyte as described above. The middle chamber was filled with a mixture of NO<sub>3</sub><sup>-</sup> and each of the corresponding interfering ion. The concentration of NO<sub>3</sub><sup>-</sup> was fixed to 2.0 × 10<sup>-5</sup> M and the concentrations of interfering ions were varied from 2.0 × 10<sup>-5</sup> to 5.0 × 10<sup>-3</sup> M where the potentials were obtained for each concentration of the interfering ions. Next, potentials were recorded for NO<sub>3</sub><sup>-</sup> ions only of the same concentrations in the absence of any interfering ion. With these

values, the selectivity coefficients were determined by the matched potential method. Interfering ions ( $= 2.0 \times 10^{-5}$  -  $5.0 \times 10^{-3}$  M) were added to the reference solution ( $= 2.0 \times 10^{-5}$  M) until the potential change from interfering ion reached the potential change caused by the primary ion. The selectivity of CSM based MISM was measured in a similar manner.  $\text{Na}^+$  and  $\text{K}^+$  were used as interfering ions.

#### 2.2.5. BPE-based colorimetric sensor fabrication

ITO-coated glass ( $7.5 \text{ cm} \times 2.5 \text{ cm}$ ) was washed with ethanol, acetone and deionized water for 10 min, respectively. Then it was baked at  $100 \text{ }^\circ\text{C}$  for 5 min. HMDS was spin coated and baked at  $110 \text{ }^\circ\text{C}$  for 1.5 min, and PR was spin coated and baked at  $100 \text{ }^\circ\text{C}$  for 1.5 min. PR was illuminated with UV light (365 nm) for 20 s while being covered with a patterned mask fabricated in the shape of the BPE (rectangular, length 6 cm, width 0.1 cm). PR is dissolved in AZ 400K developer and baked at  $120 \text{ }^\circ\text{C}$  for 15 min. The ITO was etched using etchant (TE-100) for 15 min at  $80 \text{ }^\circ\text{C}$ . PR residues were removed by washing with acetone.

The mold for PDMS cover was fabricated as the followings. Silicon wafer was cleaned with piranha solution ( $\text{H}_2\text{SO}_4:\text{H}_2\text{O}_2$  3:1) for 20 min and dried at  $200 \text{ }^\circ\text{C}$  for 2 min. After cooling, SU-8 was spin coated and baked at  $65 \text{ }^\circ\text{C}$  for 2 min and at  $95 \text{ }^\circ\text{C}$  for 7 min. UV light was illuminated on SU-8 for 20 s being covered with a patterned mask which was fabricated in the shape of the closed BPE channel (length 3.3 cm, width  $400 \text{ }\mu\text{m}$ , height  $90 \text{ }\mu\text{m}$ ). SU-8 pattern was developed by treating with SU-8 remover for 2 min. The wafer was baked at  $200 \text{ }^\circ\text{C}$  for 10 min, and at  $65 \text{ }^\circ\text{C}$  for 5 min. Mixture of PDMS monomer and curing agent (10 : 1) was poured on the patterned wafer after attaching it onto a dish and baked at  $60 \text{ }^\circ\text{C}$  for 2 h.

Ag/AgCl paste first is applied on one end of ITO (width  $400 \text{ }\mu\text{m}$ , length 2 cm, thickness  $30 \text{ }\mu\text{m}$ ) and heated at  $150 \text{ }^\circ\text{C}$  for 20 min, and PANi is electrodeposited on



the other end of ITO. For PANi electrodeposition, the ITO electrode was covered with insulating tape with 0.1 cm in diameter, and constant voltage of 0.75 V (vs Ag/AgCl) was applied to the ITO until total charge reached  $1.2 \times 10^{-4}$  C in 0.5 M aniline and 1.0 M H<sub>2</sub>SO<sub>4</sub> solution. After PANi deposition, polymerized PDMS from PDMS mold was cut into 7.5 cm  $\times$  2.5 cm and aligned along with ITO patterned glass to be attached onto it.

#### 2.2.6. Membrane charge density calculation.

DM membrane potentials are determined using two Ag/AgCl reference electrodes in the way shown in Fig. 2-3a. DMs were placed between two chambers of high and low concentrations of KCl solutions. A pump circulates the solution via the inlets and the outlets of the chamber, maintaining the concentration gradient. In detail, the measurements were conducted at flow rate of 25 ml/min, tube diameter of 1 mm, and chamber volume of 2 ml. Two salt bridges between the chamber and the 3 M KCl solution minimize any potential fluctuation. The ratio between the high ( $C_1$ ) and low ( $C_2$ ) concentrations  $r = (C_1/C_2)$  was set to 10. When the membrane charge density ( $\theta$ ) is substantially smaller compared to  $C_2$ , diffusion potential becomes the dominating factor in determining the membrane potentials as the Donnan potential becomes negligible. Thus, the cation transport number ( $t_{+}^{*}$ ) can be calculated by the steady state potential obtained at 20 mM and higher of KCl solutions.

#### 2.2.7. Hue value and pixel intensity calculation

Photograph of PANi on patterned ITO glass was taken with digital camera and central area with 0.9 mm in diameter was further analyzed as following.

First pixel values (R, G, B values) are obtained as an average of all pixels. Among the three, the maximum value (max) and the minimum value (min) are determined.

If max = R, then hue value =  $60 \times ((G - B) \div (R - \min))$

If max = G, then hue value =  $60 \times (2.0 + (B - R) \div (G - \min))$ .

If max = B, then hue value =  $60 \times (4.0 + (R - G) \div (B - \min))$ .

If the obtained hue value is negative, 360 is added. The average of the three R, G, and B values gives pixel intensity.

### 2.3. Result and Discussion

The structure of MISM is illustrated at Fig. 2-1. MISM consists of a series of membranes, reference electrolyte and sample solution, which are arranged alternatively. The membranes are either dialysis membrane (DM), which separates reference electrolytes and sample solutions, or nitrate selective membrane (NSM), which generates potential difference due to the salinity gradient between the reference electrolyte and the sample. The potential difference across one NSM is added up to that of the next NSM, and the total voltage is measured from two Ag/AgCl electrodes which are independently in contact with the first and the last reference electrolytes. One tack of MISM is composed of one pair of NSM and dialysis membrane.

NSM is fabricated by embedding nitrate selective ionophores on anion exchange membrane (AEM) mixed with poly(vinyl chloride) (PVC), a plasticizer and a lipophilic additive. PVC is one of the most classic polymeric matrices for ionophore-based ISEs, well-established, cheap, and easy to handle. A variety of commercially available ionophores can be introduced instead of nitrate selective ionophores for membranes with different selectivities. AEMs are made from robust materials thus have long been used as electro dialysis membranes, which show good attachment to

PVC, as shown by field emission scanning electron microscopy (FESEM) (Fig. 2-2a).

Cation exchange membranes (CEMs) in conventional REDs must be replaced with DMs, to make net emf depend on nitrate concentration in the sample. Therefore, cellulose ester based DM serves as the reference membrane to separate the reference electrolyte and the sample. DM needs no extra doping processes and gives reproducible results.

I tested three different types of cellulose ester based DMs with varying pore sizes for optimal reference membrane with low charge density. SEM images of three DMs with different molecular weight cut-off (MWCO) (Fig. 2-2b, c, d) show that the size and the density of the pores are proportional to MWCO of DM. The membrane charge densities of DMs were calculated from equation (1), as it was previously reported. [79] The experimental setup for the measurement of membrane charge density has a chamber that is divided into two cells by given DM as shown in Fig. 2-3a. The potential difference across the DM between the dissimilar ion concentrations in two cells was measured (Fig. 2-3 a, b, c).

$$\left(\frac{F}{RT}\right) \Delta E = (1 - 2t_+^*) \ln r - \frac{2(r-1)}{r} t_+^* (1 - t_+^*) \left(\frac{\theta}{C_2}\right) \quad (2)$$

$\Delta E$  is the membrane potential,  $t_+^*$  is the cation transport number,  $\theta$  is the membrane charge density,  $r$  is the ratio between the high ( $C_1$ ) and low ( $C_2$ ) concentrations, which was set to 10.

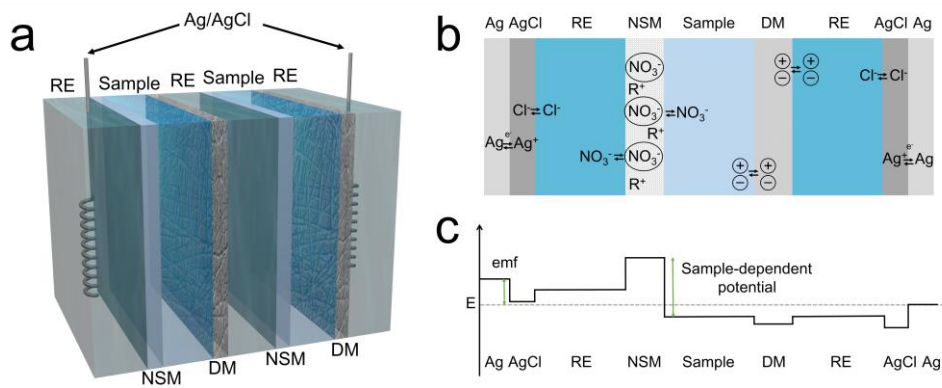


**Fig. 2-1. Schematic illustration of MISM and its electrical profile.**

a. Structure of two-stacked MISM. b. Schematic presentation of single stack MISM with relevant interfaces. c. Electrical potential profile of single stack MISM.

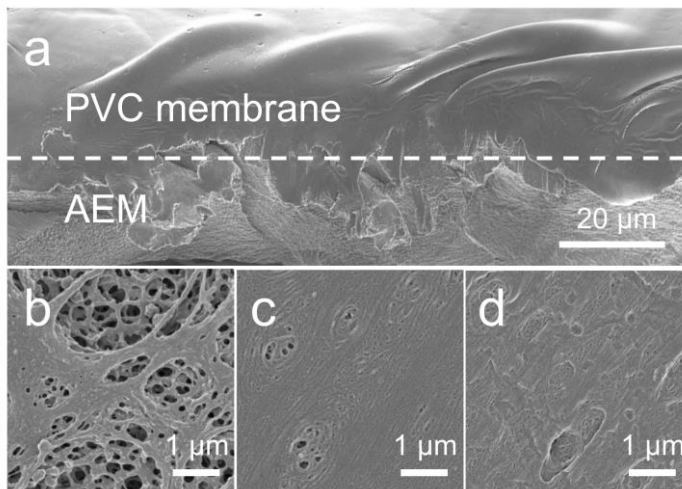


**Fig. 2-2. FESEM images of Membranes**

a. Cross-section view of NSM. Top view of b. 1,000 kDa DM, c. 100 kDa DM, and d. 10 kDa DM.

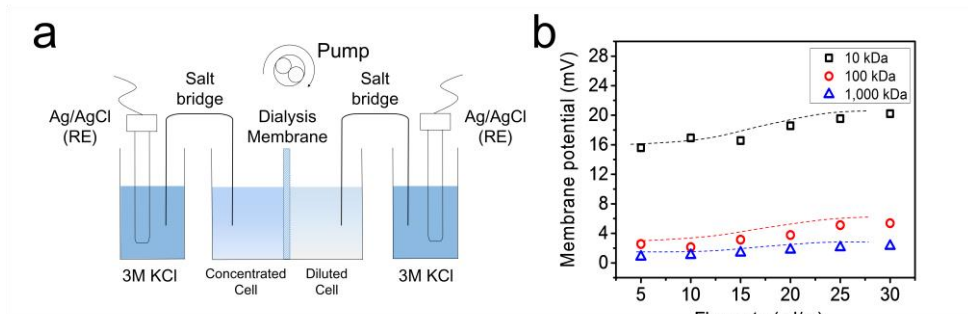


**Fig. 2-3. Measurement of membrane charge density of DM.**

a. Setup for measurement of DM charges. A dialysis membrane separates concentrated and diluted cells containing aqueous KCl solutions. An external pump keeps the concentration ratio between the two solutions constant. Ag/AgCl reference electrodes were immersed into 3 M KCl solutions and connected to the two solutions via a salt bridge. The diluted cell concentrations varies from 0.5 mM to 100 mM and the concentration ratio between the concentrated chamber and the diluted chamber is fixed to 10. b. DM potentials measured as a function of flow rate. Positive correlation between the observed potential and flow rate was obtained at 5–30 mL/min. Membrane potential was saturated at 25 mL/min, which was selected for measuring membrane charge density.

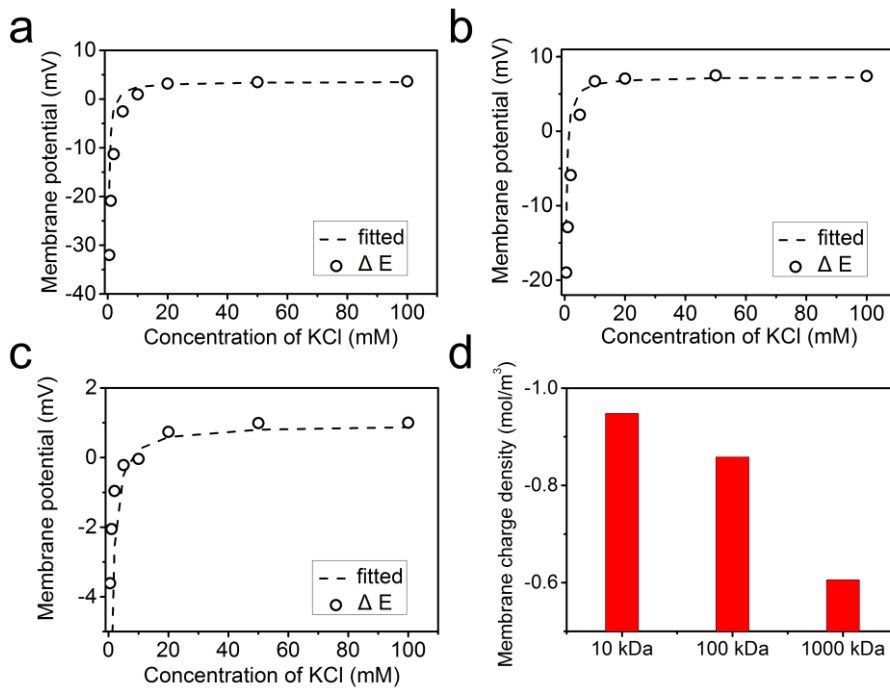


**Fig. 2-4 . Characteristics of DM with different MWCO.**

Membrane potential of a. 1000 kDa, b. 100 kDa, c. 10 kDa DM by varying the solution concentration (diluted side) and maintaining the ratio between the high and low concentration to 10. Experimental values of  $E$  at high KCl concentrations were plotted against  $1/C$  to obtain the value of charge density ( $\theta$ ). d. Membrane charge densities of DMs with different MWCO.

The measured potential was converted into membrane charge density from equation (2), with obtained steady state potential and cation transport number. Membrane charge density from three different MWCO of DM is summarized in Fig. 2-3d. The result is in good accordance with what was expected; lower MWCO of DM, denser membrane, and larger surface area of membrane give rise to the higher charge density. Membrane potential of DMs with different MWCO were measured with 10 mM nitrate as a high concentration solution and 0.05 - 5 mM nitrate as a low concentration solution. Among the three examined DMs, the voltage outcome from the 1000 kDa DM showed the smallest absolute value and variation, which means smallest potential disturbance between sample and reference electrolyte (Fig. 2-4). Therefore, I chose the DM with MWCO of 1000 kDa as a reference membrane throughout the study unless otherwise stated.

Figure 2-5a presents the potential vs. concentration plot of a single-stack device with only one NSM-DM pair, revealing that a near-Nernstian response of 57.08 mV decade<sup>-1</sup> is observed over a wide concentration range of  $6.1 \times 10^{-6} - 7.0 \times 10^{-2}$  M. The detection limit is evaluated as  $4.1 \times 10^{-6}$  M from the intersection of the two extrapolated segments of the calibration curve. The effects of  $\text{HCO}_3^-$ ,  $\text{SO}_4^{2-}$ , and  $\text{Cl}^-$ , the most common anions of natural water, on the nitrate selectivity of the single-stack MISM were probed using the matched potential method, [80] (Fig. 2-6b) and the obtained selectivity coefficients ( $3.4 \times 10^{-3}$ ,  $7.7 \times 10^{-2}$ , and  $1.1 \times 10^{-3}$ , respectively) indicated that this system was well selective for  $\text{NO}_3^-$  over major interfering ions in natural water.

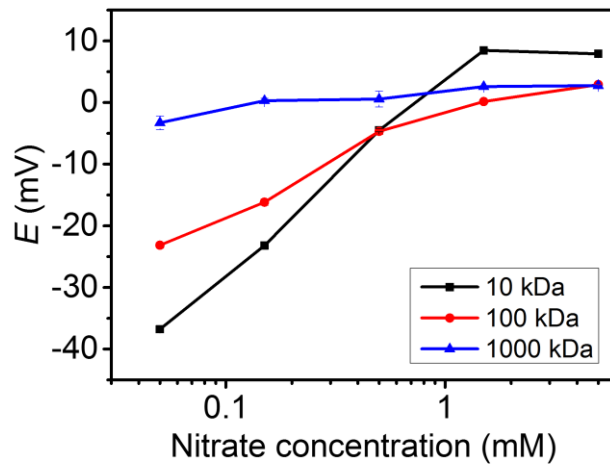


**Fig. 2-5. Membrane potential of DMs with different MWCO**

Solution concentration of one side was maintained to 10 mM  $\text{NaNO}_3$ , the other side was varied from 0.05 mM to 5 mM  $\text{NaNO}_3$ .



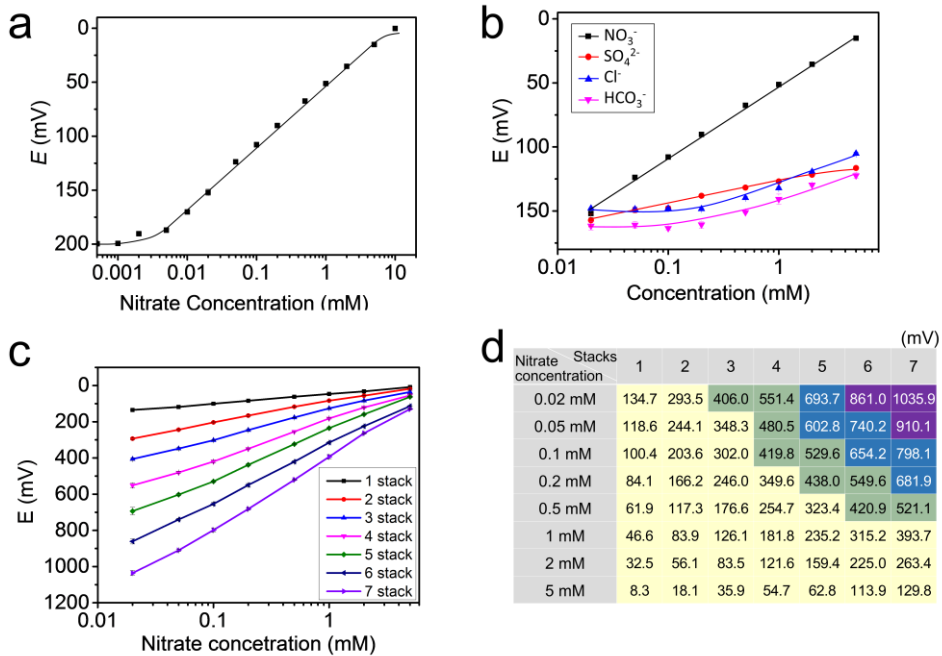


**Fig. 2-6. Characteristics and emf enhancement of MISM.**

a. Calibration curve for single stack MISM. b. Potential responses of NSM to  $\text{HCO}_3^-$ ,  $\text{SO}_4^{2-}$  and  $\text{Cl}^-$ . c. Potential-concentration response of MISM with different number of stacks, from 1 to 7. The sensitivity of MISM increases as a function of the number of stacks. d. Potential generated from 1 to 7 stack MISM. The background shows the color generated from BFE-based potentiometric sensor.

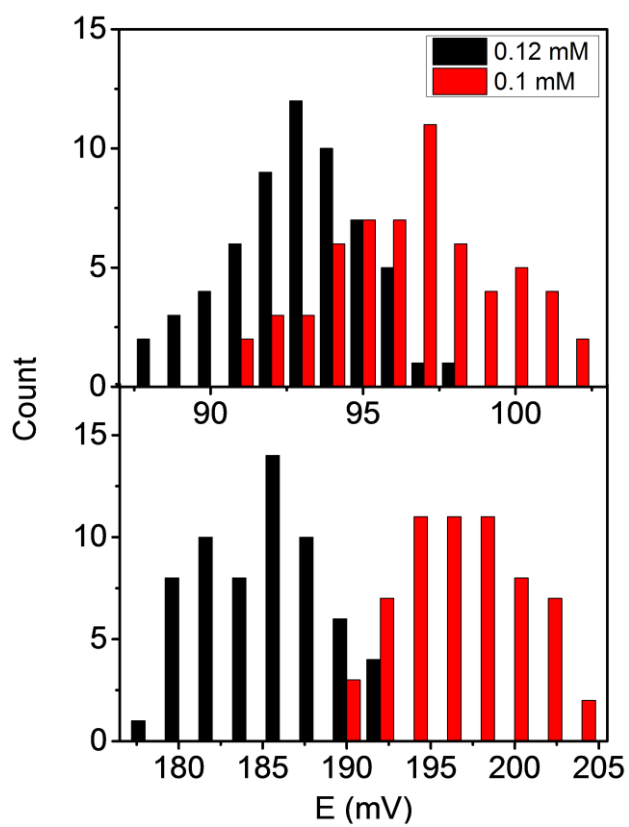


**Fig. 2-7. Voltage distribution of 1 stack (top) and 2 stack MISM (bottom) for nitrate concentration of 0.1 mM (red) and 0.12 mM (black).**

Besides being simple and disposable, the most intriguing trait of multilayer structure is that potential differences created by individual NSMs are accumulated to produce net emf in proportional to the number of NSMs as the NSM-DM pairs are stacked alternatively (Fig. 2-1). This means that I can modulate the sensitivity by simply choosing NSM-DM pairs stacks. The Nernstian slope of  $57.1 \text{ mV decade}^{-1}$  for single stack increases to  $388.1 \text{ mV decade}^{-1}$  for 7 stacks (Fig. 2-5c), showing 6.8-fold increase of sensitivity (Table 2). The potential values measured for each concentration and number of stacks are represented in the table shown in Figure 2-5d. Furthermore, the potential distribution of 0.1 mM and 0.12 mM nitrate measured with 1 stack and 2 stack MISM is shown in Figure 2-6. For the 1 stack MISM, 80.0% of total counts were included in the overlapped range, on the other hand, only 15.8% of total counts were included for the 2 stack MISM. Therefore, increased sensitivity facilitates the distinction between two adjacent concentrations, thereby achieving higher resolution of the measurement.

Moreover, the increase in sensitivity applies for not only monovalent ions, but also for multivalent ions, of which the potentiometric quantitation is commonly hindered by low sensitivity. As a demonstration,  $\text{Ca}^{2+}$ -selective membrane (CSM) based MISM was fabricated by embedding  $\text{Ca}^{2+}$ -selective ionophore into a CEM mixed with PVC and plasticizer following the method used for NSM fabrication. While the theoretical diffusion potential of a divalent ion is only  $29.5 \text{ mV decade}^{-1}$ , the obtained CSM based MISM manifested a  $\text{Ca}^{2+}$  sensitivity of  $115 \text{ mV decade}^{-1}$  for four stacks (Fig. 2-7). This value largely exceeds the conventional value by a factor of 3.90, representing a significant improvement in sensitivity. This result supports that MISMs are not limited to the sensing of monovalent anions but can be used for universal ion sensing with enhanced and tunable sensitivity.

To check MISM stability and robustness, I conducted experiments on potential equilibration and time-dependent fluctuation, revealing that the potential of a six-stack cell reaches  $\pm 1$  mV of the stabilized value within 5 s after electrolyte injection and decreases by only 1.3% after 30 s on average (Fig. 2-8). Figure 2-9 shows the effect of sample pH (3.2–8.6;  $2 \times 10^{-3}$  M nitrate solution) for a single-stack MISM, demonstrating that the potential output remains stable and largely constant at pH 3.5–7.8 and critically decreases outside this range. Figure 2-9b reveals that only insignificant MISM selectivity and potential deteriorations are observed within eight days of dry storage under ambient conditions.

**Table 5. Sensitivity of MISM as a function of the number of stacks. Nitrate concentrations from 0.02 mM to 5 mM were used to plot the trend line for sensitivity of each stack.**

Number of stacks	Sensitivity (mV decade <sup>-1</sup> )	Sensitivity enhancement compared to single stack
1	57.1	1.00
2	116.2	2.03
3	159.9	2.80
4	215.5	3.77
5	270.5	4.73
6	320.8	5.62
7	388.1	6.80

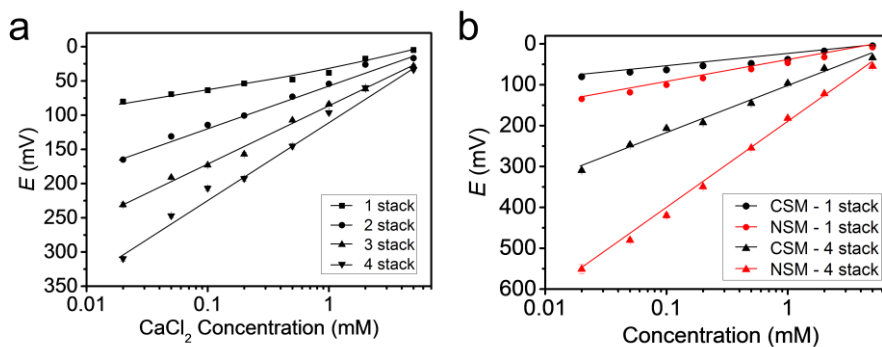


**Fig. 2-8. emf enhancement of MISIM with NSM and CSM**

a. Potential-concentration response of CSM based MISIM with different number of stacks. The sensitivities of stacks were 30.8 mV decade<sup>-1</sup>, 62.8 mV decade<sup>-1</sup>, 84.6 mV decade<sup>-1</sup>, 115 mV decade<sup>-1</sup> for 1 to 4 stacks, respectively. b. Comparison of sensitivity enhancement between CSM and NSM based MISIM. The sensitivity of CSM based 4 stack MISIM is 53.3 % of that of NSM based 4 stack MISIM, which is attributed to the valence charge of the target ion of CSM based MISIM, Ca<sup>2+</sup>, which is twice of the valence charge of NO<sup>3-</sup>. The error bars in a., b. represent  $\pm$  SD (n = 3).

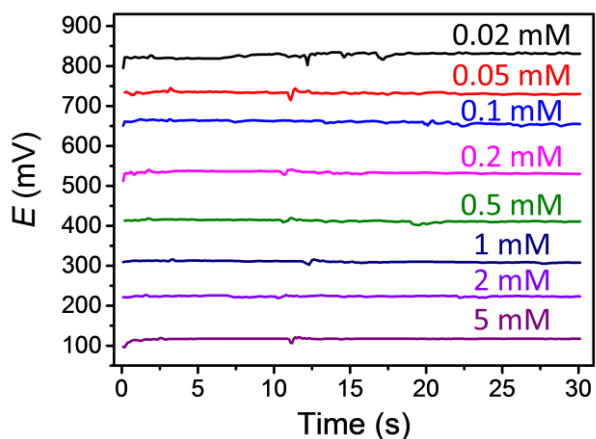


**Fig. 2-9.** The potential of a 6 stack MISM reaches  $\pm 1$  mV of the stabilized value within 5 s after the injection of the electrolyte, and the potential decreases 1.3% in 30 s on average.

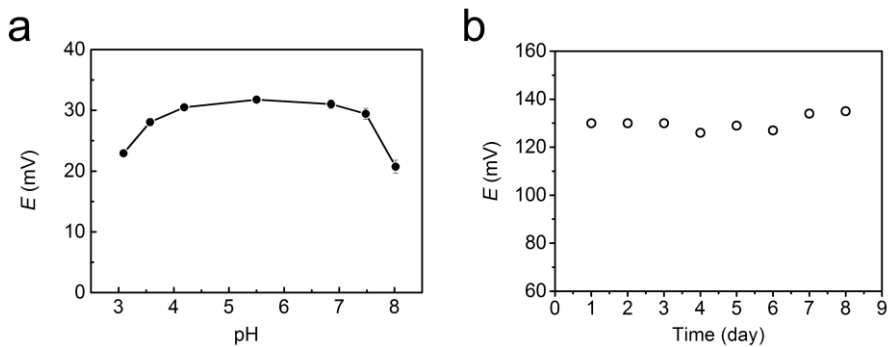
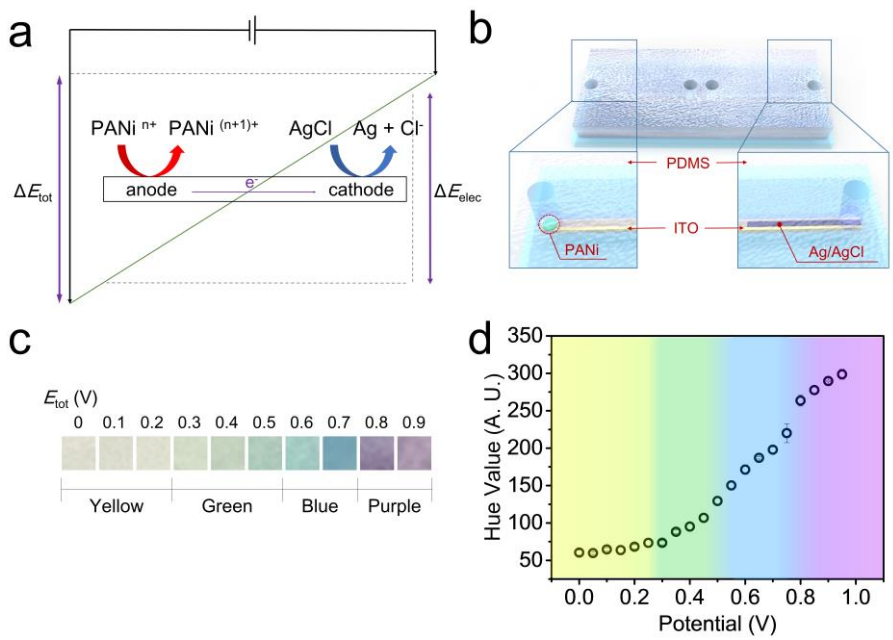


**Fig. 2-10.** Stability of single stack MISM.

a. Effect of pH on emf for a sample solution. b. Daily OCP of MISM recorded for 0.02 mM nitrate solution with 0.1 mM chloride ions. The error bars in a. represent  $\pm$  SD ( $n = 3$ ).

BPE based colorimetric detection system visualizes potential difference responsible for the nitrate concentration of sample from MISM. An Ag/AgCl is immobilized on one end of the BPE to pin the redox potential (Fig. 2-10 b). On the other end, I put electrochromic PANi that has four representative oxidation states each bearing a different color for different applied potential: yellow, green, blue and purple (Fig. 2-11). When the BPE system is connected to the MISM, the voltage generated by the MISM alters the oxidation states of PANi film, producing a characteristic color that corresponds to the potential generated from MISM. As a result, one can directly assess the ion concentration of interest in the sample by just looking the color change with naked eyes. Still, it needs no any extra power source but only a small disposable membrane stack and PANi-painted BPE to conduct quick and easy analysis on site.

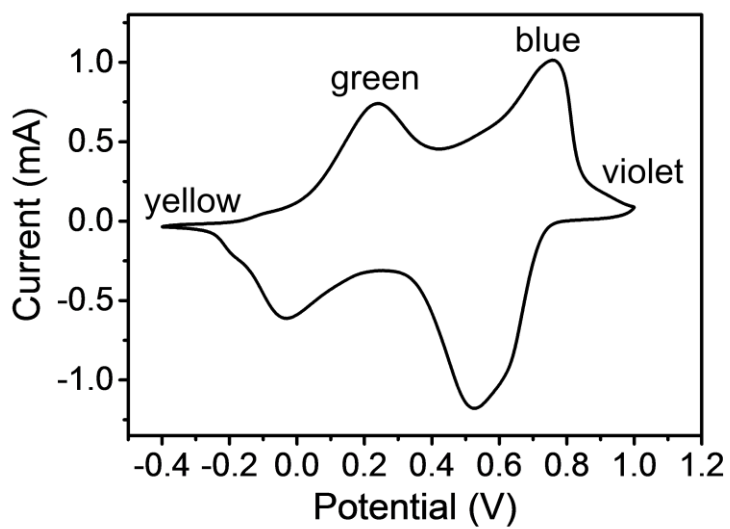
A schematic diagram of the BPE-based multicolor detection system is shown in Figure 2-10a. On one end of the BPE, electrochemical oxidation of PANi takes place to induce color change relevant to the applied potential ( $\Delta E_{\text{elec}} \sim \Delta E_{\text{tot}}$ ). Simultaneously, reduction of silver chloride occurs on the other end to retain the current equality. BPE in this study is made of indium-tin oxide on a slide glass, which is covered by polydimethylsiloxane (PDMS) with a patterned microchannel and a reservoir. Both BPE and chip are transparent and robust materials that safely allow to observe color changes (Fig. 2-10b).



**Fig. 2-11. Structure and the color of BPE-based colorimetric detection system.**

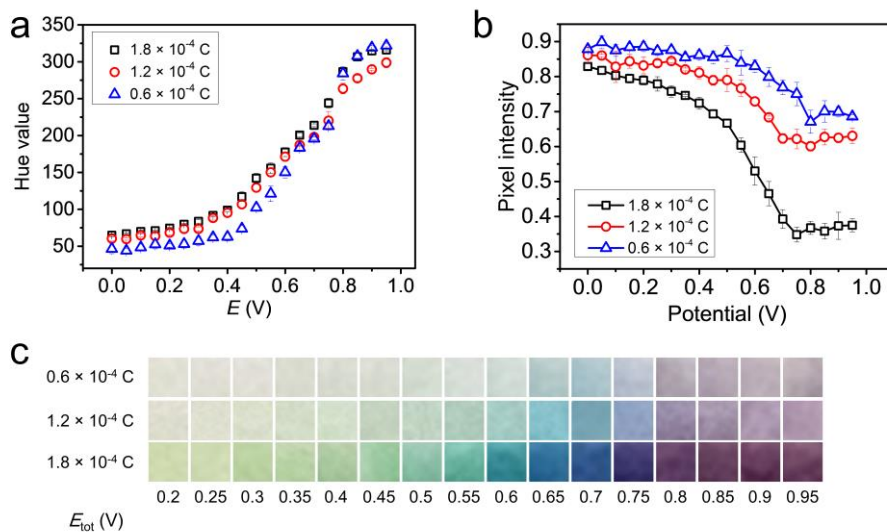
a. Schematic diagram of the BPE-based multicolor ion detection system. b. Three-dimensional structure of the bipolar electrode chip. c. PANi color chart obtained using a potentiostat. d. Hue values observed for different potentials applied by the potentiostat.





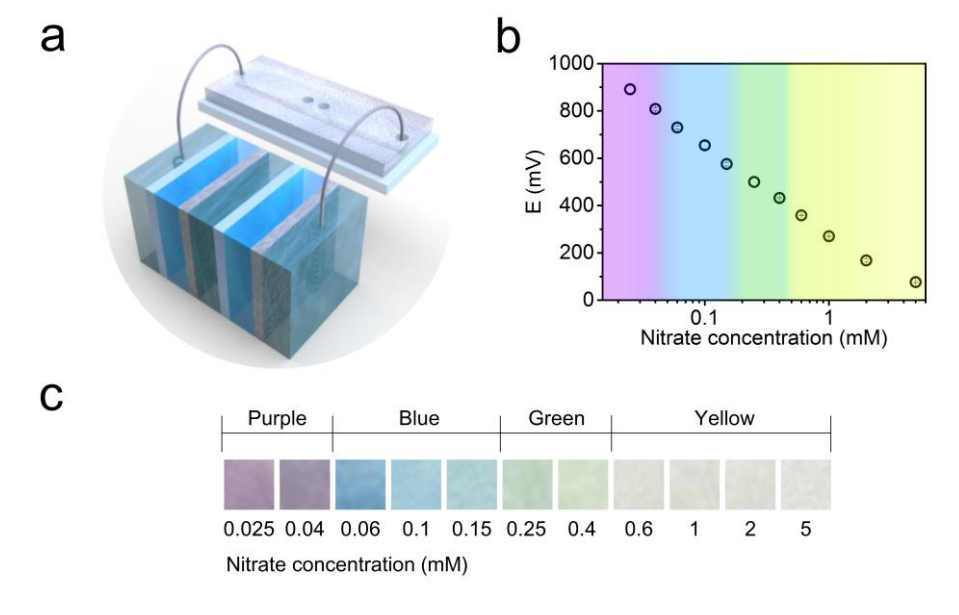
**Fig. 2-12. Cyclic voltammogram of polyaniline that has four oxidation states and respective colors.**

Figure 2-10c shows the colorimetric data at various BPE operation voltage. PANi was electrodeposited at constant potential and the charge for electrodeposition was optimized on the consideration of the response time of the sensor and clear color visualization (Fig. 2-12). The observed color changes from yellow to purple, which is distinct enough to directly determine the ion concentration level with the naked eye by collating with the color chart. Furthermore, the so-obtained color profile can be analyzed as well by converting the color change into hue values and pixel intensity. While it requires extra device like smartphone equipped with camera, such conversion can offer useful option to digitize the colorimetric information for more accurate quantitative analysis (Fig. 2-10d). I can calculate hue value [81] automatically on the basis of the mean pixel values (red, green and blue) of the image taken from a camera. Hue values take on a number between 0 and 360, which constitutes a continuous spectrum of color change from red to purple. In this experiment, hue values of 35-75, 75-165, 165-235, and 235-310 were sorted yellow, green, blue, and purple, respectively. Hue value changes gradually from yellow to blue, where sharp increase was observed from blue to purple. As found in Fig. 4f, pixel intensity can be used for further tuning the sensitivity even with black and white CCD, which could be more sensitive.



**Fig. 2-13. Hue value, Pixel intensity, and color chart according to applied potential.**

a. Observed hue values under different potentials applied by a potentiostat. b. Hue values and f. Pixel intensities based on the charges applied on PANi. c. Observed colors with various potentials and charges.



**Fig. 2-14. Combined structure and Hue value of MISM and BPE-based sensor.**

a. Combined structure of MISM (2 stack) and BPE-based multicolor and potentiometric sensor. b. Corresponding potential from different nitrate concentrations from 6 stack MISM, with the color of the background indicates the color generated from BFE-based potentiometric sensor. c. Depiction of obtained color from a series of nitrate concentrations using 6 stack MISM.

The BPE-based multicolor detection system was combined with a MISM to construct a simple, disposable, and sensitivity-tunable ion sensor (Fig. 2-13a) (The photographs of single stack MISM and BPE are shown in figure 2-17). As the range of colors provided by PANi depended on nitrate concentration and the number of stacks, the concentration range of interest could be easily modulated by changing the number of stacks (Fig. 2-5d). To test the applicability of the fabricated system to real-life samples, a six-stack MISM was employed for river water analysis. When the six-stack MISM was connected to the BPE, the MISM-generated voltage was divided according to the BPE/MISM resistance ratio. Optimization of MISM internal resistance allowed us to effectively and reliably apply the MISM-generated voltage to the BPE (for details of the optimization process, see Fig. S7). The membrane surface area was one of the parameters optimized to reduce MISM internal resistance and thus ensure effective voltage transmission to the BPE. The use of high membrane areas resulted in increased currents and hence, in more rapid PANi color changes, thus leading to shorter response times (Fig. 2-14d). To analyze the effect of unknown ions on voltage distribution, MISM internal resistance was examined in the presence of various concentrations of interfering ions. Taking into account the natural abundance of chloride ions, I measured the resistance of the six-stack MISM in 0.05 mM nitrate solution in the presence of 0.05–1 mM chloride ions, revealing that a 13.9% change in resistance brought about a 0.187% change in the potential exerted to BPE. Consequently, when the nitrate concentration increased from 0.02 to 5 mM, the color changed from purple to pale yellow, which was well discernible with the naked eye (Figs. 2-13b, c). Such color changes could be converted to the corresponding hue values, as shown in Figure 2-15.

To test if the MISM sensing platform can be used as a portable device for field tests of river water, I collected river water samples from two different spots and

analyzed them with a six-stacked MISM after filtration through a 0.02- $\mu\text{m}$  filter (Table 3). The obtained colors (blue and green) directly indicated that the nitrate concentrations in both samples did not exceed the World Health Organization (WHO) stipulated threshold values which is 0.8 mM (Fig. 2-13c). [82] The observed hue values of 199.5 and 138.1 corresponded to nitrate concentrations of 0.06–0.1 mM and 0.15–0.25 mM, respectively. To confirm the accuracy of this measurement, I used ion chromatography to determine nitrate levels in the two samples, showing that the obtained values of 0.061 and 0.211 mM were in good agreement with those provided by the MISM-BPE system. Thus, the MISM-based on-spot colorimetric analysis developed herein was concluded to be well suited for electronics- and battery-free environmental and hygiene monitoring.

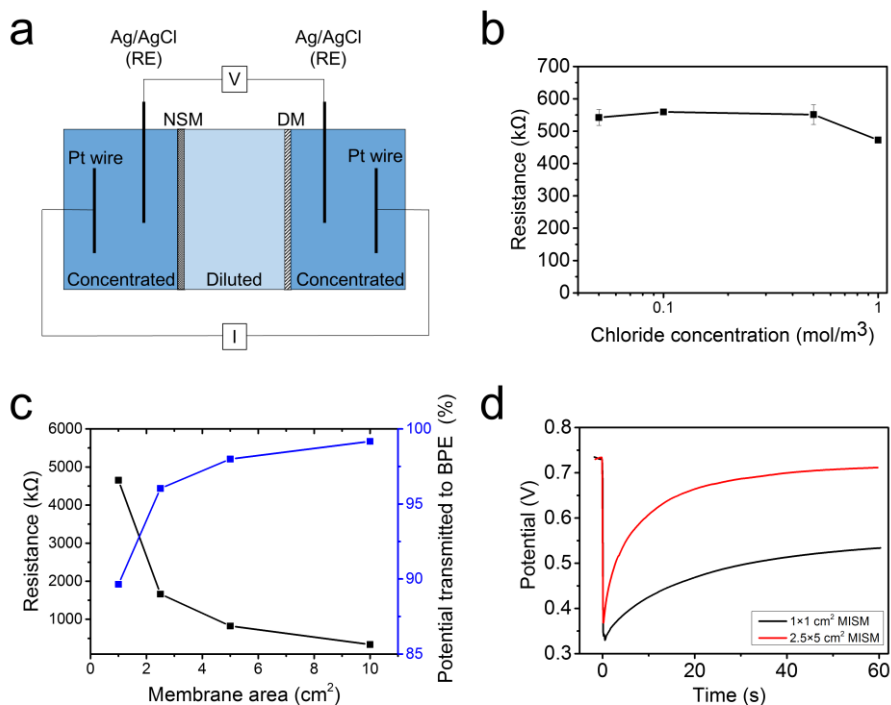


**Fig. 2-15. Resistance of MISM**

a. Scheme of membrane resistance measurement. Ag/AgCl reference electrodes were immersed in both chambers to record the potential difference. Constant current was applied to the MISM through Pt wires in the two chambers. The resistance of the MISM was calculated from the IR drop due to the current applied. b. Measured resistance for a series of chloride concentrations. c. Resistance and potential transmitted to the BPE for various membrane areas. d. Time-dependence of the potential for different MISM areas. The error bars in b, c represent  $\pm$  SD (n = 3).

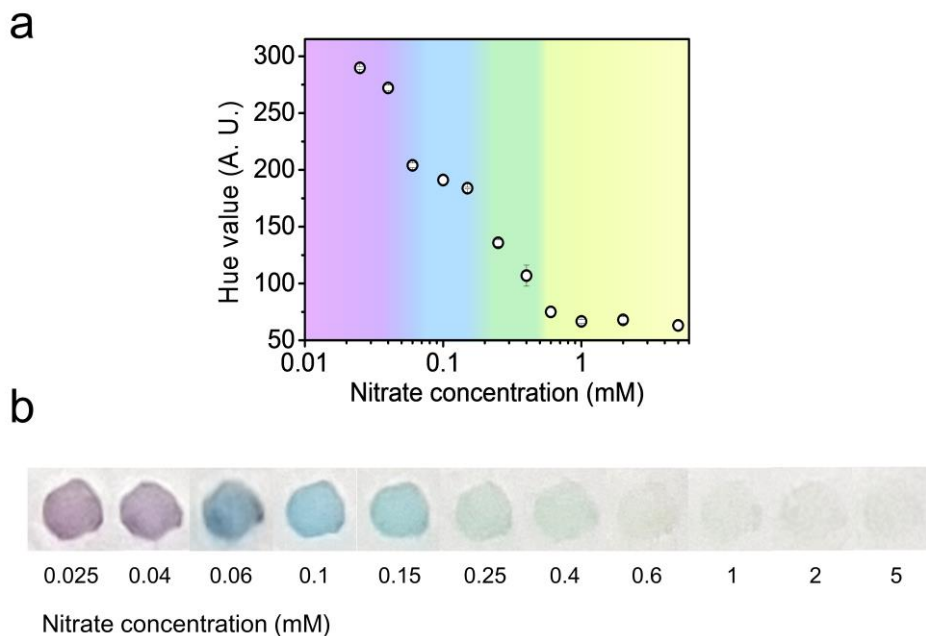




**Fig. 2-16. Hue value and colors of PANi corresponding to the nitrate concentration.**

a. Hue values for a series of nitrate concentrations. The background indicates the color generated from BPE based potentiometric sensor. b. Colors of PANi generated from six-stack MISM in response to a series of nitrate concentrations. The cropped image is shown in Fig. 5c. The error bars in a. represent  $\pm$  SD (n = 3).



**Table 6. Results of river water analysis**

	Spot A	Spot B
Ion chromatography–determined nitrate concentration	0.0610 mM	0.211 mM
MISM potential	695 mV	499 mV
Nitrate concentration determined from MISM potential	0.0764 mM	0.265 mM
Color		
Hue value	199	138
Nitrate concentration determined from hue value	0.0717 mM	0.262 mM

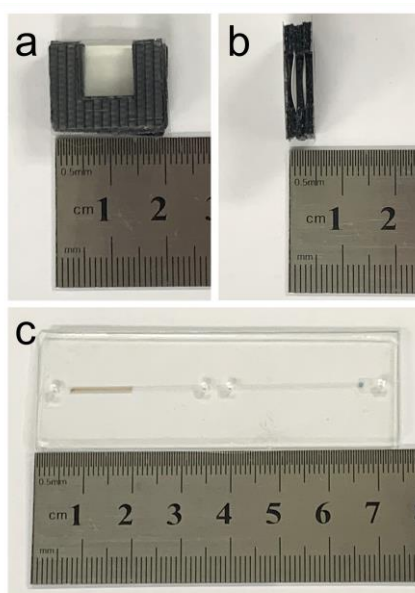


**Fig. 2-17. Photographs of a single stack MISM and BPE microchip.**

a. Front view of a single stack MISM. b. Top view of a single stack MISM c. Top view of a BPE microchip.

## 2.4. Conclusion

Herein, I adopted a non-stereotypical approach to RED systems to fabricate a novel multicolor ion-sensing platform, showing that the use of MISMs, which are modified RED systems employing ion-selective and ion-non-selective membranes, greatly expands the scope of both conventional RED and ion-sensing technologies. Moreover, MISMs were demonstrated to serve as power generators driving the entire system and as selective signal producers for ion concentration in a given sample. Potentiometric sensitivity practically exceeded the Nernstian slope and could be modulated by simple variation of the number of NSM-DM stacks constituting the MISM. MISM integration with a bipolar electrode (BPE) yielded a disposable, convenient, and sensitive ion-sensing platform. The presence of a MISM obviated the need for an external power source and gave rise to a continuous color gradient of PANi film on BPE, enabling swift super-sensitive quantitation with the naked eye and allowing hue value digitization for data storage and further analysis. Besides nitrate, which was used as an example in this study, other ions can be targeted by simply selecting the relevant ionophores. Moreover, the MISM-based ion-sensing concept can also be implemented in the construction of parallel systems for multiplex analysis, which reveals the immense potential of the RED technology for future applications such as highly versatile self-powered ion sensors.

## 2.5. References

- [57] R. E. PATTLE, "Production of Electric Power by mixing Fresh and Salt Water in the Hydroelectric Pile," *Nature*, vol. 174, no. 4431, pp. 660–660, Oct. 1954.
- [58] J. Jagur-Grodzinski and R. Kramer, "Novel process for direct conversion of free energy of mixing into electric power," *Ind. Eng. Chem. Process Des. Dev.*, vol. 25, no. 2, pp. 443–449, Apr. 1986.
- [59] X. Tong, B. Zhang, and Y. Chen, "Fouling resistant nanocomposite cation exchange membrane with enhanced power generation for reverse electrodialysis," *J. Memb. Sci.*, vol. 516, pp. 162–171, Oct. 2016.
- [60] Z. He, X. Gao, Y. Zhang, Y. Wang, and J. Wang, "Revised spacer design to improve hydrodynamics and anti-fouling behavior in reverse electrodialysis processes," *Desalin. Water Treat.*, vol. 57, no. 58, pp. 28176–28186, Dec. 2016.
- [61] E. Guler, Y. Zhang, M. Saakes, and K. Nijmeijer, "Tailor-Made Anion-Exchange Membranes for Salinity Gradient Power Generation Using Reverse Electrodialysis," *ChemSusChem*, vol. 5, no. 11, pp. 2262–2270, Nov. 2012.
- [62] D. A. Vermaas, M. Saakes, and K. Nijmeijer, "Power generation using profiled membranes in reverse electrodialysis," *J. Memb. Sci.*, vol. 385–386, pp. 234–242, Dec. 2011.
- [63] S. Fujii, K. Takeichi, and M. Higa, "Optimization of RED Test Cell for PVA Based Ion-Exchange Membranes," *Procedia Eng.*, vol. 44, pp. 1300–1302, Jan. 2012.
- [64] J. Veerman, M. Saakes, S. J. Metz, and G. J. Harmsen, "Reverse electrodialysis: Performance of a stack with 50 cells on the mixing of sea and river water," *J. Memb. Sci.*, vol. 327, no. 1–2, pp. 136–144, Feb. 2009.
- [65] M. Turek, B. Bandura, and P. Dydo, "Power production from coal-mine brine utilizing reversed electrodialysis," *Desalination*, vol. 221, no. 1–3, pp. 462–466, Mar. 2008.
- [66] M. Tedesco *et al.*, "Reverse electrodialysis with saline waters and concentrated brines: A laboratory investigation towards technology scale-up," *J. Memb. Sci.*, vol. 492, pp. 9–20, Oct. 2015.
- [67] X. Zhu, W. He, and B. E. Logan, "Influence of solution concentration and salt types on the performance of reverse electrodialysis cells," *J. Memb. Sci.*, vol. 494, pp. 154–160, Nov. 2015.

- [68] E. Brauns, "Salinity gradient power by reverse electrodialysis: effect of model parameters on electrical power output," *Desalination*, vol. 237, no. 1–3, pp. 378–391, Feb. 2009.
- [69] R. D. Cusick, Y. Kim, and B. E. Logan, "Energy Capture from Thermolytic Solutions in Microbial Reverse-Electrodialysis Cells," *Science (80-. )*, vol. 335, no. 6075, pp. 1474–1477, Mar. 2012.
- [70] Y. Mei and C. Y. Tang, "Co-locating reverse electrodialysis with reverse osmosis desalination: Synergies and implications," *J. Memb. Sci.*, vol. 539, pp. 305–312, Oct. 2017.
- [71] J. Lee, J. Yun, S.-R. Kwon, W. J. Chang, K. T. Nam, and T. D. Chung, "Reverse Electrodialysis-Assisted Solar Water Splitting," *Sci. Rep.*, vol. 7, no. 1, p. 12281, Dec. 2017.
- [72] S. R. Kwon *et al.*, "Electrodeless Reverse Electrodialysis Patches as an Ionic Power Source for Active Transdermal Drug Delivery," *Adv. Funct. Mater.*, vol. 28, no. 15, pp. 1–10, 2018.
- [73] S. H. Han, S.-R. Kwon, S. Baek, and T.-D. Chung, "Ionic Circuits Powered by Reverse Electrodialysis for an Ultimate Iontronic System," *Sci. Rep.*, vol. 7, no. 1, p. 14068, Dec. 2017.
- [74] S. Y. Yeon *et al.*, "A miniaturized solid salt reverse electrodialysis battery: a durable and fully ionic power source," *Chem. Sci.*, vol. 9, no. 42, pp. 8071–8076, Oct. 2018.
- [75] S. E. Fosdick, K. N. Knust, K. Scida, and R. M. Crooks, "Bipolar Electrochemistry," *Angew. Chemie Int. Ed.*, vol. 52, no. 40, pp. 10438–10456, Sep. 2013.
- [76] F. Mavr e *et al.*, "Bipolar Electrodes: A Useful Tool for Concentration, Separation, and Detection of Analytes in Microelectrochemical Systems," *Anal. Chem.*, vol. 82, no. 21, pp. 8766–8774, Nov. 2010.
- [77] M.-S. Wu, D.-J. Yuan, J.-J. Xu, and H.-Y. Chen, "Electrochemiluminescence on bipolar electrodes for visual bioanalysis," *Chem. Sci.*, vol. 4, no. 3, p. 1182, Feb. 2013.
- [78] Y. Zhu, T. Tsukamoto, and S. Tanaka, "On-chip electrochromic micro display for a disposable bio-sensor chip," *J. Micromechanics Microengineering*, vol. 27, no. 12, p. 125012, Dec. 2017.
- [79] K. Yamamoto *et al.*, "Membrane potential and charge density of hollow-fiber dialysis membranes," *J. Memb. Sci.*, vol. 355, no. 1–2, pp. 182–185, Jun. 2010.

- [80] K. Tohda, D. Dragoë, M. Shibata, and Y. Umezawa, "Studies on the matched potential method for determining the selectivity coefficients of ion-selective electrodes based on neutral ionophores: experimental and theoretical verification," *Anal. Sci.*, vol. 17, no. 6, pp. 733–43, Jun. 2001.
- [81] K. Cantrell, M. M. Erenas, I. de Orbe-Payá, and L. F. Capitán-Vallvey, "Use of the Hue Parameter of the Hue, Saturation, Value Color Space As a Quantitative Analytical Parameter for Bitonal Optical Sensors," *Anal. Chem.*, vol. 82, no. 2, pp. 531–542, Jan. 2010.
- [82] P. Zhou, Z. Ansems, N. Torfs, "A Global Assessment of Nitrate Contamination in Groundwater," 2015.